Journal of Materials Chemistry A

ROYAL SOCIETY OF CHEMISTRY

REVIEW

View Article Online
View Journal



Cite this: DOI: 10.1039/d6ta02166b

# Electrochemical nitrate reduction to ammonia by non-noble metal single-atom catalysts: bridging waste remediation and sustainable hydrogen storage

Yongtao Xue,[a] Xiufang He[b] and Jia Wei Chew *[a]

Ammonia plays a pivotal role in agriculture and industry, while being increasingly viewed as a carbon-free hydrogen carrier. Over the past decade, electrochemical nitrate reduction to ammonia has emerged as a promising green route, bridging waste remediation and effective hydrogen storage. In this context, non-noble metal single-atom catalysts (SACs) are particularly attractive due to their tunable electronic structure and high reaction selectivity. This review provides a timely and comprehensive overview of electrochemical nitrate reduction to ammonia by non-noble metal SACs. In this review, the principles and reactor configurations for electrochemical nitrate reduction are examined and then the synthesis strategies and characterization techniques for non-noble metal SACs are critically summarized. Recent advances in utilizing non-noble metal single-atom catalysts for electrochemical nitrate reduction to ammonia are systematically assessed in terms of $NH_3$ yield, Faraday efficiency, selectivity, and underlying mechanisms. Finally, the persistent challenges and future perspectives are discussed, with the aim of guiding the rational design of non-noble metal single-atom catalysts towards highly efficient electrochemical nitrate reduction to ammonia.

Received 12th March 2026
Accepted 10th May 2026

DOI: 10.1039/d6ta02166b

rsc.li/materials-a



## 1. Introduction

Ammonia ($NH_3$) is an essential chemical product and indispensable industrial feedstock globally, with extensive applications in agriculture and industry (*e.g.*, nitrogen-containing polymers and dyes). Notably, approximately 80% of ammonia production is consumed as agricultural fertilizer.[1,2] At present, global nitrogen-based fertilizer production is estimated at 150 million tons and is projected to increase steadily at around 2.3%, primarily driven by population growth, rising food demand, and food security.[3] Beyond its agronomic importance, $NH_3$ is gaining interest as a promising zero-carbon energy carrier for sustainable hydrogen storage, owing to its inherent advantages, including a high hydrogen mass fraction (17.6%), high energy density (4.25 kWh $L^{-1}$), easy liquefaction (10 bar or −33 °C), and well-established methods for storage and transport.[4,5] However, industrial $NH_3$ synthesis remains mainly reliant on the conventional Haber–Bosch process, which requires harsh conditions of elevated temperatures (400–500 °C) and high pressures (10–30 MPa).[6] This energy-intensive process consumes approximately 1–2% of the global energy supply and results in excessive $CO_2$ emissions (420 Mt $year^{-1}$), corresponding to around 1.5% of total greenhouse gas emissions.[7,8] Therefore, amid escalating energy and climate pressures, the development of sustainable, low-carbon and environmentally benign alternatives for industrial $NH_3$ production is both urgent and necessary.

To date, electrochemical methods have been widely explored as promising alternatives for $NH_3$ production since they can offer efficient and cost-effective synthesis under mild operating conditions.[9] In particular, the utilization of nitrates as the nitrogen source provides an attractive waste-to-value strategy that simultaneously addresses nitrate-contaminated water remediation and sustainable ammonia generation. This approach is motivated by the fact that nitrate is a ubiquitous water pollutant that can trigger eutrophication, pose risks to human health (*e.g.*, methemoglobinemia and thyroid dysfunction), and disrupt the balance of the natural N-cycle.[10,11] As illustrated in Fig. 1a, electrochemical nitrate reduction to ammonia has therefore become an active and rapidly growing research area. The challenge lies in the intrinsic complexity of electrochemical nitrate reduction to ammonia, involving the generation of multiple intermediates and byproducts (*e.g.*, $NO_2^-$, NO, and $NH_2OH$). In addition, the competing hydrogen evolution reaction (HER) inevitably occurs, which can significantly compromise Faraday and nitrate conversion efficiencies.[12] Hence, the development of catalysts with high selectivity

[a]Department of Chemistry and Chemical Engineering, Chalmers University of Technology, Gothenburg, 412 96, Sweden. E-mail: jia.chew@chalmers.se
[b]Dipartimento di Chimica, Università degli Studi di Milano, Via Golgi 19, Milan, 20133, Italy

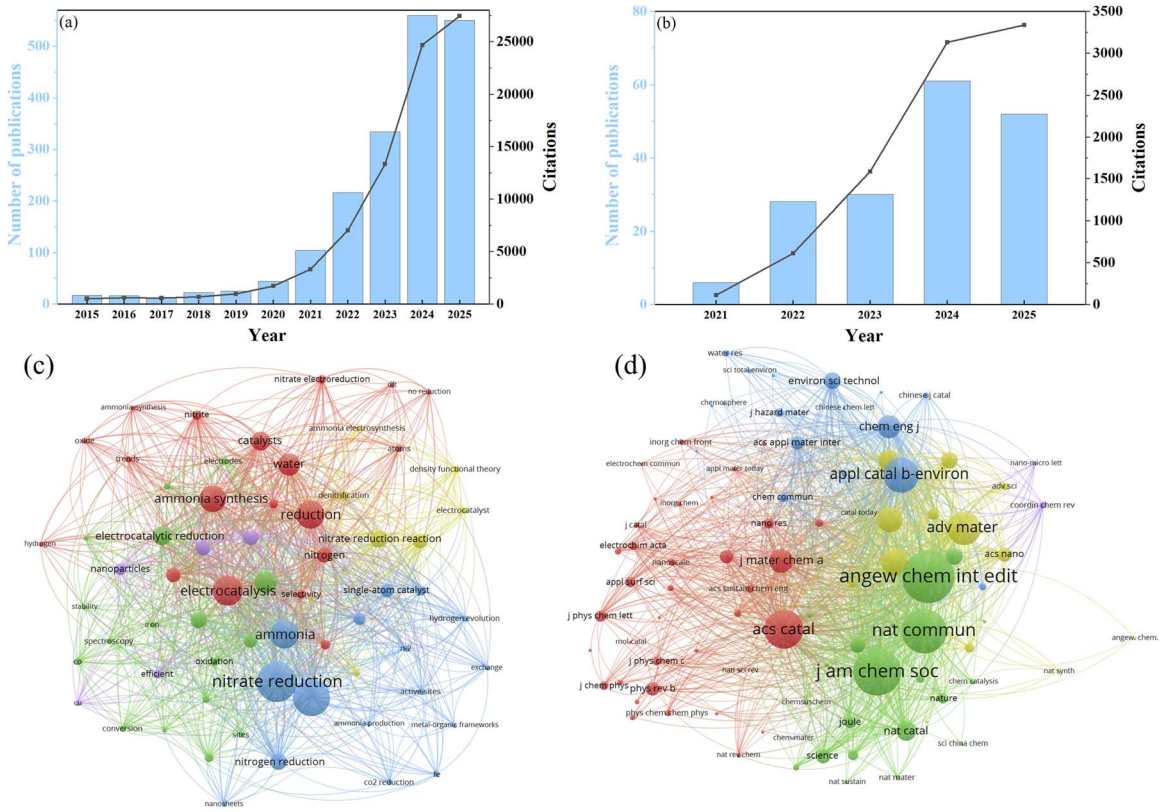


Fig. 1 The number of publications and citations on the different topics: (a) electrochemical nitrate reduction to ammonia and (b) electrochemical nitrate reduction to ammonia by non-noble metal single-atom catalysts. (c) Keywords, and (d) co-citation analysis on the topic of electrochemical nitrate reduction to ammonia by non-noble metal single-atom catalysts through VOSviewer (the data were obtained from the Web of Science on November 25, 2025).

toward $NH_3$ and excellent conversion efficiency is highly desirable for practical electrochemical nitrate reduction.

In response to this need, a variety of catalysts have been investigated for electrochemical nitrate reduction to ammonia, such as $Cu_{7.2}S_4/CoS_2$ composites,[13] IrNi alloy nanobranches,[14] $Cu_9S_5$ sub-nanowires,[15] $Cu/Cu_2O/Co_3O_4$ heterostructures,[16] Fe single-atoms coupled with carbon-shell-coated FeP nanoparticles,[17] and Ag single-atoms anchored on g-$C_3N_4$.[18] Among these catalysts, single-atom catalysts (SACs) have emerged as particularly attractive candidates due to their nearly 100% metal atom utilization, tunable electronic structures, and well-defined active sites, which collectively enable superior catalytic performance for electrocatalytic nitrate reduction.[19,20] Given the scarcity and high cost of noble metals (*e.g.*, Pt and Pd), increasing attention has been directed to non-noble metal SACs (*e.g.*, Fe- and Cu-based SACs). As a result, the development of non-noble metal SACs for electrochemical nitrate reduction to ammonia, together with the elucidation of the underlying mechanisms, has attracted considerable research interest (Fig. 1b). As shown in Fig. 1c, keyword analysis demonstrates that current studies primarily focus on ammonia yield and nitrate reduction efficiency, while co-citation analysis highlights the interdisciplinary nature of this field, spanning chemistry themes (*e.g.*, *Journal of the American Chemical Society*), materials themes (*e.g.*, *Advanced Materials*), and environmental themes (*e.g.*, *Applied Catalysis B: Environment and Energy*). To accelerate progress in non-noble metal SACs for electrochemical ammonia synthesis, a comprehensive and up-to-date review is therefore essential to consolidate current understanding and provide guidance for future research directions.

In view of the growing interest in SACs and electrochemical nitrate reduction, several reviews have surveyed related aspects, such as electrochemical nitrate reduction by cobalt catalysts,[21] noble- and non-noble metal-based catalysts for electrochemical nitrate reduction,[9] a broad overview of electrochemical nitrate reduction,[2] Fe SACs for electrochemical ammonia synthesis,[3] and non-noble metal SACs for energy-conversion reactions.[22] Nevertheless, a comprehensive review dedicated to the preparation and characterization of non-noble metal SACs and their specific application and performance in electrochemical nitrate reduction to ammonia remains lacking. In this review, the fundamentals of electrochemical nitrate reduction to ammonia, with an emphasis on reaction pathways, evaluation metrics, and reactor configurations, are introduced, followed by the synthesis strategies and characterization techniques for non-noble metal SACs. Subsequently, the performance and mechanisms for electrochemical nitrate reduction to ammonia by non-noble metal SACs are comprehensively overviewed. Finally, the key challenges are discussed and future perspectives are proposed.

 

## 2. Electrochemical nitrate reduction: fundamentals and reactor configurations

Electrochemical nitrate reduction to ammonia is intrinsically complex because nitrogen can adopt a wide range of valence states from −3 to +5. As a result, nitrate reduction involves various electron transfer pathways and generation of different intermediates, with $N_2$ and $NH_3$ being thermodynamically the most favored products.[23] Based on the overall stoichiometry, $NO_3^-$ reduction to $NH_3$ follows an eight-electron pathway (eqn (1)), whereas $NO_3^-$ reduction to $N_2$ only requires five electrons (eqn (2)). This lower electron demand makes $N_2$ formation kinetically competitive relative to $NH_3$ during nitrate reduction.[24]

$$NO_3^- + 9H^+ + 8e^- \rightarrow NH_3 + 3H_2O,\ E^0 = -0.12\ \text{V}\ \textit{vs.}\ \text{SHE}\ (1)$$

$$2NO_3^- + 12H^+ + 10e^- \rightarrow N_2 + 6H_2O,\ E^0 = 1.17\ \text{V}\ \textit{vs.}\ \text{SHE}\ (2)$$

Electrochemical nitrate reduction can generally be classified into direct and indirect pathways. The indirect reaction can only occur in the presence of high nitrate concentrations (>1 mol $L^{-1}$) and low pH levels, whereby nitrate does not participate in electron transfer during the reduction.[25] Because most reported studies have been based on low nitrate conditions, direct reaction mechanisms are considered the main pathways for electrochemical nitrate reduction and are therefore emphasized in this review. In a typical direct pathway, aqueous $NO_3^-$ ($NO_3^-{}_{(aqs)}$) first adsorbs on the electrode surface to form $NO_3^-{}_{(ads)}$ species (adsorbed state, eqn (3)), and then the N–O bond in $NO_3^-{}_{(ads)}$ is cleaved to form $NO_2^-{}_{(ads)}$ through electron transfer (eqn (4)). The conversion of $NO_3^-{}_{(ads)}$ to $NO_2^-{}_{(ads)}$ step is widely regarded as rate-limiting, because electron transfer into the lowest unoccupied molecular orbital (LUMO) of $NO_3^-$ is energetically unfavorable.[26] As illustrated in Fig. 2a, under acidic conditions, the $NO_2^-{}_{(ads)}$ can react rapidly with hydrogen ions in the electrolyte to generate $NO_{(ads)}$ (eqn (5)), followed by hydrogenation to $NH_2OH_{(ads)}$ (eqn (6)), and finally $NH_{3(ads)}$ (eqn (7)).[27] Under neutral or alkaline conditions, atomic hydrogen ($H_{(ads)}$), which is produced from water through the Volmer process (eqn (8)),[28] is involved in nitrate reduction. Owing to the strong reducing capacity ($E^0(H^+/H) = -2.31$ V *vs.* SHE), $H_{(ads)}$ can effectively reduce the adsorbed intermediates (*e.g.*, $NO_3^-{}_{(ads)}$, $NO_2^-{}_{(ads)}$, and $NO_{(ads)}$) to generate $N_{(ads)}$ (eqn (9)–(11)),[29] before finally forming $NH_{3(ads)}$ (eqn (12)). It has also been verified that $NH_{3(ads)}$ is the main product in this process, because the formation of the N–H bond by $H_{(ads)}$ is more favorable than the formation of the N–N bond.[24] Furthermore, electrochemical nitrate reduction typically involves one or multiple pathways, strongly depending on reaction conditions, including electrocatalytic electrocatalyst type, electrolyte composition, and applied potential. Consequently, rational optimization of operating conditions, together with mechanistic understanding, is crucial for further improving nitrate-to-ammonia conversion efficiency.

$$NO_{3(aqs)}^- \rightarrow NO_{3(ads)}^- \quad (3)$$

$$NO_{3(ads)}^- + 2H^+ + 2e^- \rightarrow NO_{2(ads)}^- + H_2O \quad (4)$$

$$NO_{2(ads)}^- + 2H^+ + e^- \rightarrow NO_{(ads)} + H_2O \quad (5)$$

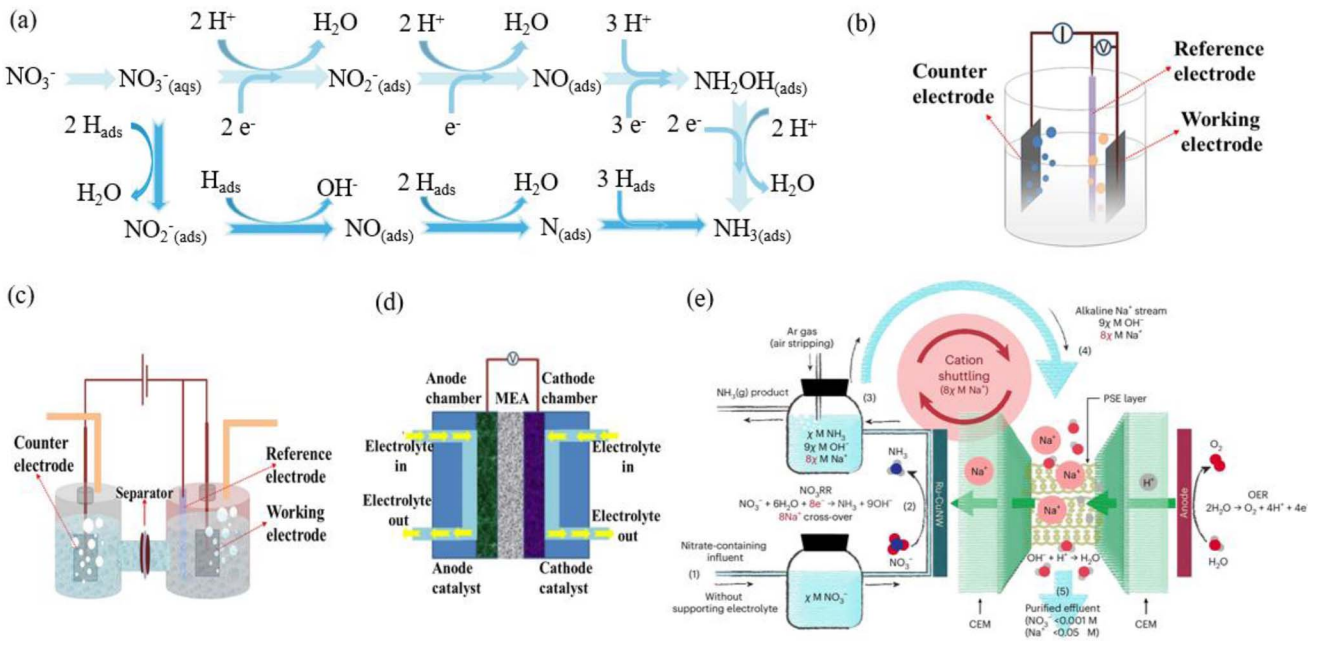


Fig. 2 (a) The main mechanisms for electrochemical nitrate reduction to ammonia; schematic illustrations of reactors: (b) single-chamber cell, (c) H-type cell, and (d) membrane electrode assembly (MEA)-based cell, reproduced with permission.[30] Copyright 2024, Elsevier. (e) Porous solid electrolyte (PSE) reactor, reproduced with permission.[36] Copyright 2024, Springer Nature.

$$NO_{(ads)} + 3H^+ + 3e^- \rightarrow NH_2OH_{(ads)} \quad (6)$$

$$NH_2OH_{(ads)} + 2H^+ + 2e^- \rightarrow NH_{3(aqs)} + H_2O \quad (7)$$

$$H_2O + e^- \rightarrow H_{(ads)} + OH^- \quad (8)$$

$$NO_{3(ads)}{}^- + 2H_{(ads)} \rightarrow NO_{2(ads)}{}^- + H_2O \quad (9)$$

$$NO_{2(ads)}{}^- + H_{(ads)} \rightarrow NO_{(ads)} + OH^- \quad (10)$$

$$NO_{(ads)} + 2H_{(ads)} \rightarrow N_{(ads)} + H_2O \quad (11)$$

$$N_{(ads)} + 3H_{(ads)} \rightarrow NH_{3(ads)} \quad (12)$$

In addition, electrochemical reactor configuration also plays an important role in the electrochemical nitrate reduction process. Commonly used reactors can be broadly classified into three categories, namely, single-chamber cells (Fig. 2b), H-type cells (Fig. 2c), and membrane electrode assembly (MEA)-based cells (Fig. 2d).[30] In the single-chamber cell, nitrate reduction occurs at the cathode while the oxygen evolution reaction occurs at the anode at an appropriate applied potential. Because the cathode and anode are not separated, the produced $NH_3$ is mixed with the generated hydrogen and oxygen in the reactor. In addition, since $NH_3$ can be re-oxidized at the anode, the faradaic efficiency for $NH_3$ is reduced.[31] Despite these limitations, single-chamber cells offer practical advantages, including lower internal resistance, simple configuration, and easy operation, making them fast, convenient platforms for preliminary performance testing. For more reliable quantification, H-type cells are employed. In this configuration, the anode and cathode are separated by a polymeric membrane (*e.g.*, the Nafion membrane), which restricts the migration of anions to the anode chamber, side reactions (*e.g.*, re-oxidation), and mixing of generated products, which collectively improve the production efficiency of ammonia.[32] An additional advantage is the operational flexibility, allowing two different wastewaters to be treated simultaneously due to the separated chambers. For instance, nitrate reduction to ammonia can occur in the cathodic chamber while the anodic chamber is used for oxidation and mineralization of organic pollutants, which can significantly reduce the energy demand for wastewater treatment.[33] However, H-type cells typically suffer from higher internal resistance because of the distance between the anode and cathode, which limits overall efficiency. To address this, membrane electrode assembly (MEA)-based cells have been explored. In an MEA configuration, the electrolytes (*e.g.*, nitrate-containing solution) are fed into the anodic and cathodic chambers separately. The direct contact between the electrode and electrolyte not only enhances the utilization of the active sites on the electrode surface but also reduces transport resistance. The generated products can be easily separated because of the presence of an ionic exchange membrane, and long-term electrolysis is enabled.[34] For instance, Boppella *et al.*[35] reported an MEA system for nitrate-to-ammonia electrolysis delivering a high $NH_3$ yield of 5.7 mmol $h^{-1}$ $cm^{-2}$ with stable operation over 100 h. Beyond these established designs, emerging reactor concepts are being developed to further improve electrochemical nitrate reduction efficiency. As illustrated in Fig. 2e, Chen *et al.*[36] developed a novel three-chamber porous solid electrolyte reactor with cation shielding effects, which can be applied for efficient nitrate reduction in the absence of supporting electrolytes. This system exhibited excellent ammonia faradaic efficiency (>90%) for high nitrate concentrations (2000 ppm), highlighting a promising design for the concurrent production of $NH_3$ and treatment of nitrate-containing wastewater.

## 3. Single-atom catalysts: comparison of synthesis strategies

Developing facile and scalable methods for the synthesis of non-noble metal SACs with excellent catalytic performance is essential for accelerating their practical deployment. However, agglomeration during synthesis presents a major challenge due to the high surface energy of single metal atoms. Consequently, considerable effort has been devoted to innovating methods that both generate atomically dispersed sites and stabilize them on suitable supports. Generally, the synthesis strategies can be classified into bottom-up and top-down approaches. In bottom-up synthesis (*e.g.*, the wet chemical method, atomic layer deposition, and electrochemical deposition), mononuclear metal precursors are dispersed or adsorbed onto the support to form SACs.[37] In contrast, top-down synthesis involves metal nanoparticles or bulk metals as the main precursors, which are often treated at high temperatures (*e.g.*, pyrolysis) or with mechanical stresses (*e.g.*, ball-milling) to isolate single atoms.[38] In this section, the key principles, strengths and limitations of various synthesis methods for non-noble metal SACs are comprehensively summarized.

### 3.1 Wet chemical method

The wet chemical method has been widely used for the synthesis of SACs, mainly due to the facile preparation steps and high potential for large-scale production. Typically, this strategy involves three main steps. First, the metal precursor is immobilized onto the substrate through various methods such as wet impregnation, deposition–precipitation, coprecipitation, and ion exchange. Subsequently, the resulting products are dried to remove the solvent and then calcined. Lastly, a reduction or activation step is applied for the formation of SACs.[39] As illustrated in Fig. 3a, Ni single-atoms dispersed on N-doped carbon nanotubes (Ni-SACs/N-CNTs) were synthesized through three main steps, involving preparation of $Ni^{2+}$/g-$C_3N_4$ through impregnation of $Ni^{2+}$ cations into g-$C_3N_4$ solution, synthesis of Ni nanoparticles/N-doped carbon nanotubes *via* pyrolysis, and then the formation of Ni single-atom/N-doped carbon nanotubes through acid-leaching and reduction.[40] Similarly, Zeng *et al.*[41] synthesized ruthenium and copper single atoms on polymeric carbon nitride through a facile preassembly-coprecipitation-pyrolysis strategy. For such methods, the heteroatoms (*e.g.*, N, S, and O) or defects in the substrates generally serve as anchoring sites for the metal ions; thus, the density and availability of these sites directly constrain the

 

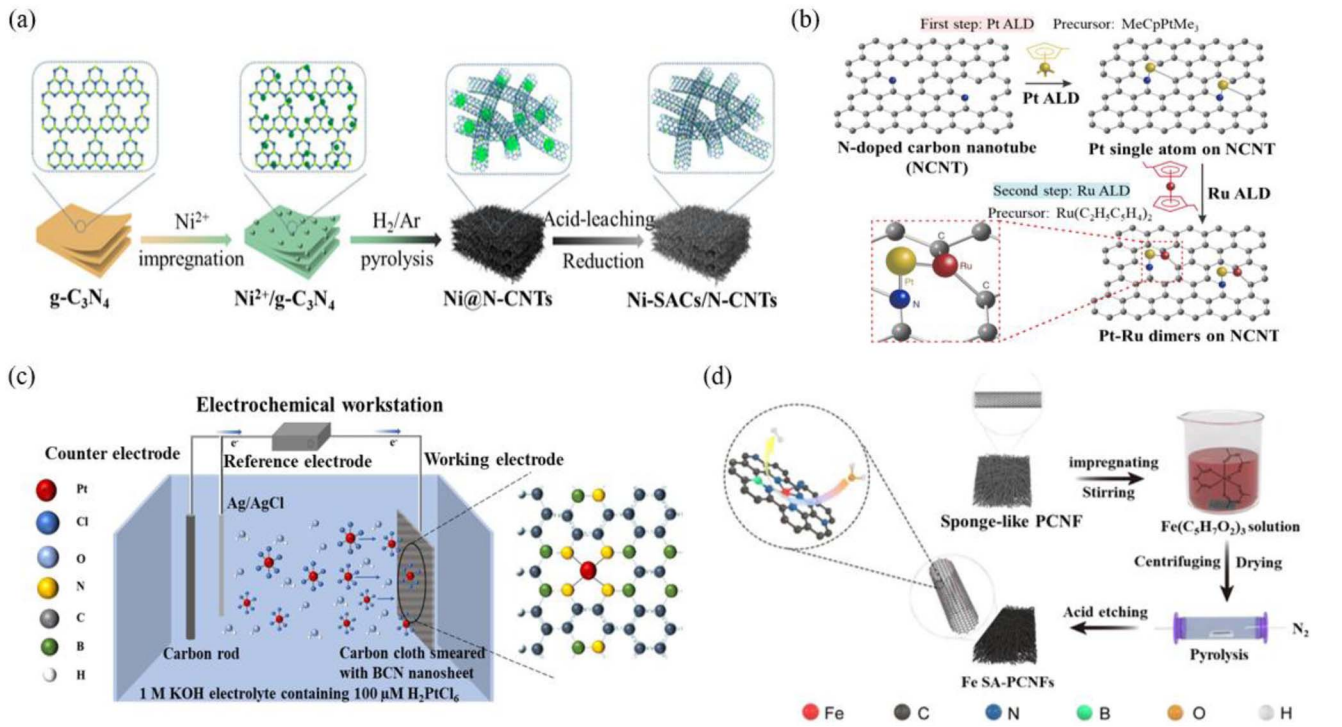


Fig. 3 (a) Schematic illustration of the SAC preparation process through the wet chemical method, reproduced with permission.[40] Copyright 2023, American Chemical Society. (b) Atomic layer deposition (ALD) method, reproduced with permission.[47] Copyright 2019, Springer Nature. (c) Electrodeposition method, reproduced with permission.[50] Copyright 2023, Elsevier. (d) Pyrolysis method, reproduced with permission.[54] Copyright 2022, American Chemical Society.

loading of SACs. In addition, the high agglomeration tendency of SACs at high metal loadings further limits the loading of SACs. Therefore, the main disadvantage of the wet chemical method for the synthesis of SACs is relatively low SAC loadings (below 1 wt%) on the supporting materials.[42] To increase single-atom loading while retaining dispersion, it is therefore desirable to (i) engineer supports with a high density of strong anchoring motifs, (ii) strengthen metal–support interactions, and (iii) precisely control key synthesis parameters.

### 3.2 Atomic layer deposition method

Atomic layer deposition (ALD) is a technique in which gaseous precursors are deposited onto solid substrates. The synthesis of SACs benefits from the ability to precisely control the loading by altering the number of ALD cycles.[43] For instance, Wang *et al.*[44] prepared Fe SACs/$SiO_2$ with different Fe single-atom loading amounts by varying the number of ALD deposition cycles. Moreover, ALD enables advantages such as homogeneous deposition layers and surface selectivity.[45] As an example, Wang *et al.*[46] synthesized $Co_1Cu$ single-atom alloys (Co single atoms were selectively coordinated to the oxygen vacancy sites on the $Cu_2O(111)$ surface) *via* site-selective ALD. Beyond monometallic SACs, ALD is also well-suited for the synthesis of two hetero single-metal atoms. As illustrated in Fig. 3b, Pt–Ru dual-metal dimers were sequentially deposited onto nitrogen-doped carbon nanotubes through ALD.[47] Despite these advantages, several practical limitations hinder large-scale implementation of ALD-derived SACs. ALD is generally time-consuming and requires relatively expensive equipment, high-cost precursors, and ultrahigh vacuum conditions. The high dissociation barriers of the metal precursors can lead to low metal loading (typically lower than 2 wt%), while formation of nanoparticles during synthesis may be unavoidable. To increase the metal loading on the substrate while retaining atomic dispersion, improving the dissolution of precursors and strengthening the chemical binding between the precursors and substrates are effective ways.[48]

### 3.3 Electrodeposition method

Electrodeposition, an electrochemical technique, is attractive for the synthesis of SACs because it is facile, low-cost, and typically conducted under mild conditions. In this approach, dissolved metal ions are electrochemically reduced at the cathode and subsequently deposited onto the substrate from an electrolyte. The loading amount and density of active sites of SACs can be accurately controlled by tailoring the synthetic parameters, including applied potential, current density, electrolyte composition, metal precursor concentration, and deposition time.[49] Notably, electrodeposited SACs are often located on the external surface of supporting materials, which enhances atom utilization during catalysis. As shown in Fig. 3c, Pt single atoms were deposited onto boron-nitride-carbon using a standard three-electrode system, yielding excellent oxygen reduction activity in fuel-cell tests.[50] This method has also been extended to the synthesis of non-noble metal SACs. For instance, Zhao *et al.*[51] prepared Cu single

atoms/covalent organic frameworks through the electrodeposition of Cu metal ions (0.1 mol $L^{-1}$ $CuSO_4$ and 0.5 mol $L^{-1}$ $H_2SO_4$ solution as electrolyte) into a covalent organic framework film-covered electrode. Similarly, Xu *et al.*[52] reported that Cu single atoms were deposited in sulfur and nitrogen co-doped graphite foam through underpotential deposition and demonstrated that the Cu single-atom loading could be modulated by tuning the deposition potential. Some limitations of electrodeposition remain unresolved. The method favors highly conductive supports, limiting the range of compatible substrates. In addition, uniform deposition of SACs is challenging, because of sensitivity to various operating parameters (*e.g.*, current and electrolyte), the lack of control of which can lead to over-deposition and agglomeration of SACs on the substrates, leading to poor catalytic performance.

### 3.4 Pyrolysis method

Pyrolysis is a facile, robust, and scalable method for the preparation of SACs. Typically, suitable precursors are thermally decomposed at a high temperature (*e.g.*, 600–1000 °C) under specific atmospheric conditions (*e.g.*, Ar, $H_2$, and $NH_3$) to isolate metal atoms and anchor them onto supporting materials.[53] The high temperatures promote direct doping or strong coordination of the metal atoms with the supporting material, resulting in highly stable SACs. However, excessively high temperatures may also promote the migration and agglomeration of isolated metal atoms, leading to the formation of clusters or nanoparticles. Post-treatment (*e.g.*, acid treatment) has been employed to remove excess metal species and preserve isolated single-atom sites. As an example, Li *et al.*[54] synthesized Fe single atom/N-doped porous nanofibers through facile pyrolysis (800 °C, $N_2$ atmosphere), followed by HCl etching (Fig. 3d), demonstrating that acid treatment effectively removed Fe particles and uniformly dispersed Fe single atoms onto the supporting materials. In addition, the pyrolysis parameters can be precisely controlled to alleviate the agglomeration of prepared SACs. For instance, Guo *et al.*[55] prepared nitrogen-doped carbon-supported Ni SACs through rapid pyrolysis (1000 °C, 90 s), with the instantaneous high temperature resulting in rapid decomposition of carbon-based precursors and vigorous evolution of gases. Gases increase internal pressure, thereby mitigating the agglomeration of Ni SACs and uniformly distributing SACs onto the nitrogen-doped carbon. Furthermore, precursor type also plays a critical role in the synthesis of SACs *via* pyrolysis. Recently, diverse precursors, including metal–organic frameworks, polymers, and small molecules, have been investigated for the preparation of SACs. For instance, Fe SACs/carbon nitride with an ultrahigh Fe loading (16 wt%) was prepared through a two-step pyrolysis strategy using melamine, cyanuric acid, and ferric acetylacetonate as the main precursors.[56] Likewise, Ni SACs/N-rich carbon matrices were obtained from zeolite imidazolate framework (ZIF)-8 *via* pyrolysis.[57] However, it should be noted that the high energy consumption associated with the high temperature and the agglomeration tendency of SACs restrict wider application of this method.

### 3.5 Ball-milling method

Ball milling has emerged as an effective approach for SAC synthesis because it is operationally simple, potentially enables high metal loading, and offers advantages in environmental compatibility (*e.g.*, no requirement for solvent) and scalability. During milling, mechanical forces break the chemical bonds of precursors to form SACs.[58] As illustrated in Fig. 4a, Cu SACs/N-doped carbon was synthesized through a two-step ball-mill process, resulting in an ultrahigh yield of SACs (around 4.2 g catalyst for each pot (70 mL volume)) and thus underscoring the potential for large-scale production.[59] Tang *et al.*[60] also observed that Ni SACs were uniformly dispersed on g-$C_3N_4$ *via* ball-mill synthesis and further emphasized that the uniformity of active sites, rather than the loading amount of SACs, can be decisive for photocatalytic performance. In addition, ball-milling can be used as an effective complementary method to prepare SACs with high performance. For instance, Liu *et al.*[61] prepared Zn–Co-MOF *via* ball-milling, and then the Co SACs/carbon were synthesized by using Zn–Co-MOF as a sacrificial template *via* pyrolysis (Fig. 4b). Similarly, Fe SACs/N-doped carbon,[62] Fe SACs/graphitic flake,[63] and Ce SACs/nitrogen-doped carbon[64] were prepared through ball-milling-assisted synthesis strategies. Aside from the advantages, it should be noted that the structures of supporting materials may be damaged during prolonged ball-milling. The reaction conditions are also difficult to precisely control, resulting in relatively low repeatability compared to other methods. More importantly, the substantial energy requirement of ball-milling limits its industrial-scale implementation for the synthesis of SACs.

### 3.6 Other strategies

Photochemical routes provide efficient pathways for SAC synthesis. In these methods, which can be implemented in either liquid or solid phases, the metal precursors can be reduced into single atoms under ultraviolet light irradiation.[65] In liquid-phase photochemical synthesis, metal precursors are frozen (*e.g.*, using liquid nitrogen) into an ice matrix, which inhibits the nucleation of products and promotes the formation of SACs during ice-melting under irradiation. In contrast, solid-phase photochemical synthesis can inhibit the agglomeration of SACs and is attractive for large-scale production because it can avoid post-processing steps such as washing and drying.[53] As illustrated in Fig. 4c, Zhang *et al.*[66] prepared Ni SACs/CdS (the Ni loading amount was 2.85%) through a facile and rapid photochemical method and demonstrated outstanding stability and durability throughout the photocatalytic hydrogen evolution reaction (HER). Similarly, Zhao *et al.*[67] anchored Co single atoms onto an MXene substrate through ice-assisted photochemical reduction.

Microwave-assisted synthesis, as a facile and environmentally friendly technique, can also be applied for the synthesis of SACs. Microwave-assisted preparation of SACs has some inherent advantages, including less reaction time and low agglomeration of SACs. For instance, Wen *et al.*[68] prepared Ni SACs/N-doped carbon by using Ni-ZIF-8 as the precursor through facile microwave-assisted pyrolysis within 3 min

 

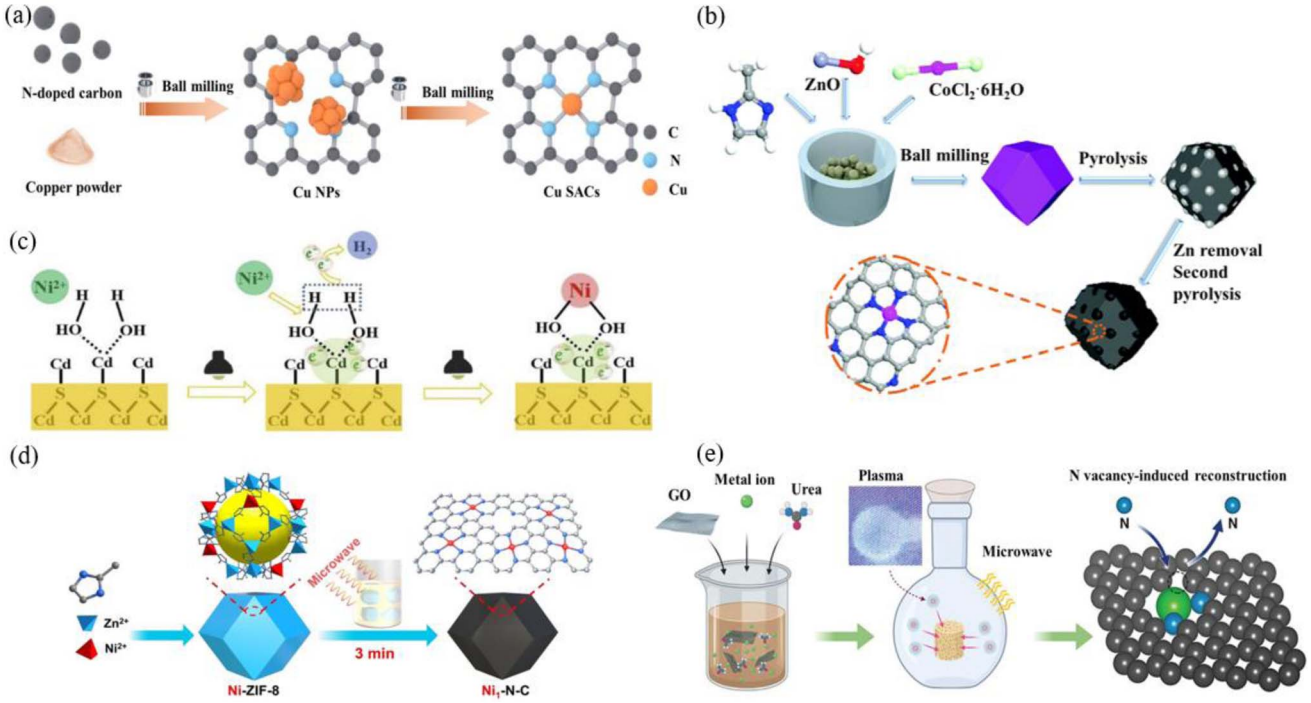


Fig. 4 Schematic illustration of the SAC preparation: (a) ball-milling process, reproduced with permission.[59] Copyright 2023, Springer Nature. (b) Ball-milling assisted process, reproduced with permission.[61] Copyright 2022, The Royal Society of Chemistry. (c) Photochemical method, reproduced with permission.[66] Copyright 2020, Elsevier. (d) Microwave-assisted process, reproduced with permission.[68] Copyright 2024, Wiley-VCH. (e) Microwave-induced plasma treatment process, reproduced with permission.[72] Copyright 2021, Wiley-VCH.

(Fig. 4d), demonstrating a fast and scalable synthesis method for SACs. Similarly, Fe and Ni dual SACs on nitrogen porous carbon materials were prepared through microwave-assisted adsorption and subsequent pyrolysis, resulting in nanocomposites with a large specific surface area and abundant active sites.[69]

Plasma-assisted methods represent another platform for SAC synthesis, often delivering highly dispersed and enriched active sites compared to conventional heating methods.[70] For instance, Rao *et al.*[71] prepared Fe SACs/carbon support through plasma bombing, which enabled direct transformation of metal precursors into isolated atomic sites. This strategy is promising for the scalable production of SACs with different metals. As shown in Fig. 4e, Ni SACs with nitrogen vacancies were synthesized through microwave-induced plasma treatment, which facilitated removal of nitrogen atoms, resulting in the reconstruction of active sites.[72]

# 4. Characterization of non-noble metal single-atom catalysts

Beyond synthesis strategies, advanced characterization techniques also play a key role in the study of coordination environments and atomic dispersion of the prepared non-noble metal SACs. At present, existing characterization methods for non-noble metal SACs can be mainly classified into two categories, namely, microscopy-based (*e.g.*, scanning transmission electron microscopy (STEM) and scanning tunneling microscopy (STM)) and spectroscopy-based (*e.g.*, X-ray absorption spectroscopy (XAS), X-ray photoelectron spectroscopy (XPS), and electron paramagnetic resonance (EPR)). In this section, the advantages and limitations of various characterization methods for non-noble metal SACs are discussed. It is important to emphasize that no single technique is sufficient to definitively characterize SACs. Because different methods probe distinct spatial scales and possess inherent constraints, a combination of complementary techniques is generally required to comprehensively identify isolated single atom sites and their local coordination environments.

## 4.1 STEM

Conventional scanning electron microscopy (SEM) and transmission electron microscopy (TEM) are valuable for characterizing size and morphology, but are generally regarded as indirect or assistant methods due to the limited resolution. Recently, high-angle annular dark-field STEM (HAADF-STEM) has been shown to directly visualize the morphology of SACs at an atomic resolution (0.1 nm). In HAADF-STEM, differential scattering of electrons on the detector causes atoms with high and low atomic numbers to appear on the resulting images respectively as bright and dark regions. Because metal sites have much higher atomic numbers than supporting materials (*e.g.*, carbon materials), they can be discerned as bright regions.[73] For instance, Jiang *et al.*[74] observed *via* SEM and TEM that the prepared Cu SACs-nitrogen doped carbon demonstrated a crimped sheet-like porous structure with abundant folds (Fig. 5a and b), but these images could not confirm the

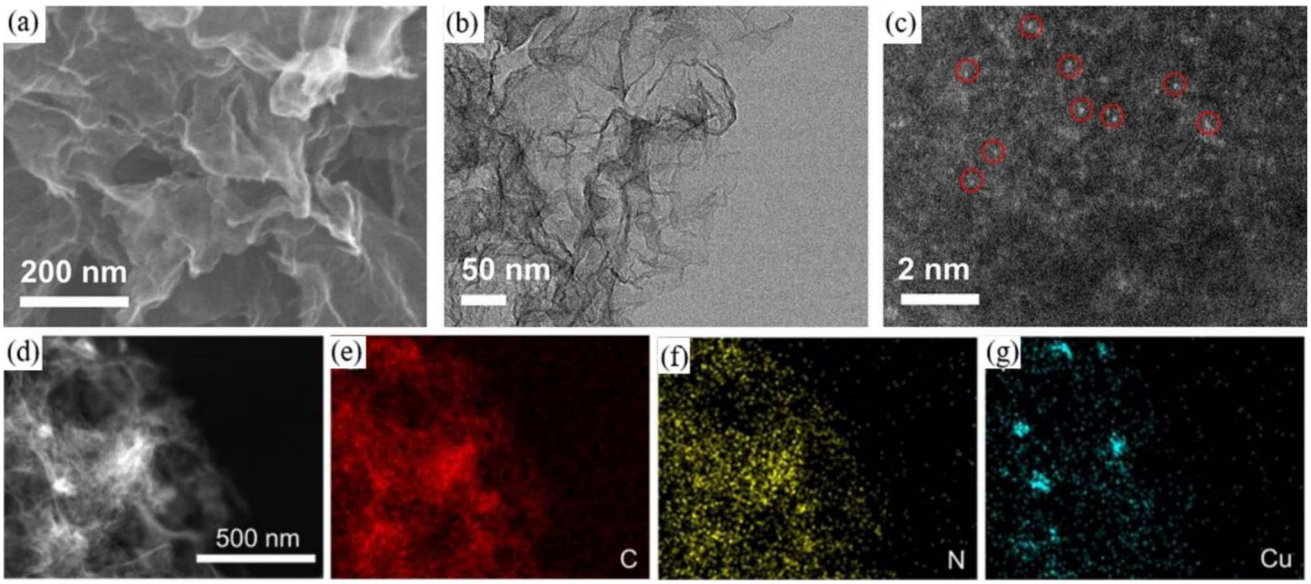


Fig. 5 (a) SEM, (b) TEM, (c and d) HADDF-STEM image, and (e–g) corresponding elemental mapping of Cu SACs-nitrogen doped carbon, reproduced with permission.[74] Copyright 2023, Wiley-VCH.

presence of SACs. In contrast, HAADF-STEM and corresponding elemental mapping results (Fig. 5c–g) indicate Cu SACs as bright spots (highlighted by red circles in Fig. 5c) and their uniform dispersion on the nitrogen-doped carbon carriers. However, it remains challenging to distinguish SACs through HAADF-STEM if the substrate materials contain metal sites with similar atomic numbers. In addition, HAADF-STEM is not suitable for quantitative analysis of SACs since the observation is typically limited to selected local regions rather than statistically representative data of the entire sample.[75]

### 4.2 XAS

X-ray absorption spectroscopy (XAS) reveals the electronic structure and local coordination environment of SACs. Under X-ray irradiation, the inner electrons of the atom can be excited into the continuum, with the resulting photoelectrons behaving as waves backscattered from neighboring atoms. The interference between the outgoing and backscattered waves, either in phase or out of phase, leads to the characteristic oscillations observed in XAS spectra, thereby providing fingerprint information of the specified element.[76] According to the relative energy, XAS can be classified as X-ray absorption near-edge structure (XANES, 30–50 eV) and extended X-ray absorption fine structure (EXAFS, 50–1000 eV). XANES is highly sensitive to the chemical state of the absorbing atom, including the oxidation state and coordination species, while EXAFS provides information on the bonding environment of SACs, such as the coordination number and chemical bond length.[77] EXAFS and XANES are analyzed together to provide information about the chemical environment for SACs, and inconsistencies in the same sample indicate artificial interference. Generally, EXAFS is used to determine the coordination number and bond distances, based on which XANES can be applied to investigate valence states and electronic structures. However, the distinguishing of light-atom scattering from metal–metal contributions (such as M–N or M–C) is limited when these features overlap in *R* space. To address this, WT-EXAFS provides simultaneous resolution in both *R* and *k* space, which allows for reliable differentiation of scattering paths from lighter neighboring atoms and heavier metal atoms. As an example, Guo *et al.*[78] observed that the adsorption edge position of Co SACs/carriers was 7717.5 eV, which is similar to the position of CoO (7717.9 eV), suggesting that the oxidation state was +2 (Fig. 6a). Fig. 6b shows that the characteristic peak of Co SACs (1.6 Å) was ascribed to the first shell of the Co–O band, and no characteristic peaks of Co–Co were observed, suggesting the successful preparation of Co SACs. The EXAFS fitting results (Fig. 6c and d) indicate that the average coordination number was 4 in Co SACs. In addition, the WT-EXAFS (Fig. 6e) demonstrate that only one peak was observed at a position of 1.6 $Å^{-1}$, which is related to the atomic Co–O coordination. No Co–Co bonds were determined in Co SACs/carriers, suggesting the absence of Co clusters and nanoparticles.

Although XAS is a very useful technique for the characterization of SACs, there are also some limitations. The relatively low loading of SACs on the substrate results in weak XAS signals, thereby requiring long acquisition times for signals or high-brightness X-ray sources. In addition, XAS can only provide average data for SACs, making it difficult to resolve local structural heterogeneity or determine the specific position distribution of single atoms.

### 4.3 XPS

X-ray Photoelectron Spectroscopy (XPS), an advanced technique, has been extensively used for investigating elemental compositions and valence states of materials and for distinguishing the SACs and metal oxides based on the difference in electron states. As an example, Guo *et al.*[79] observed Co SACs

 

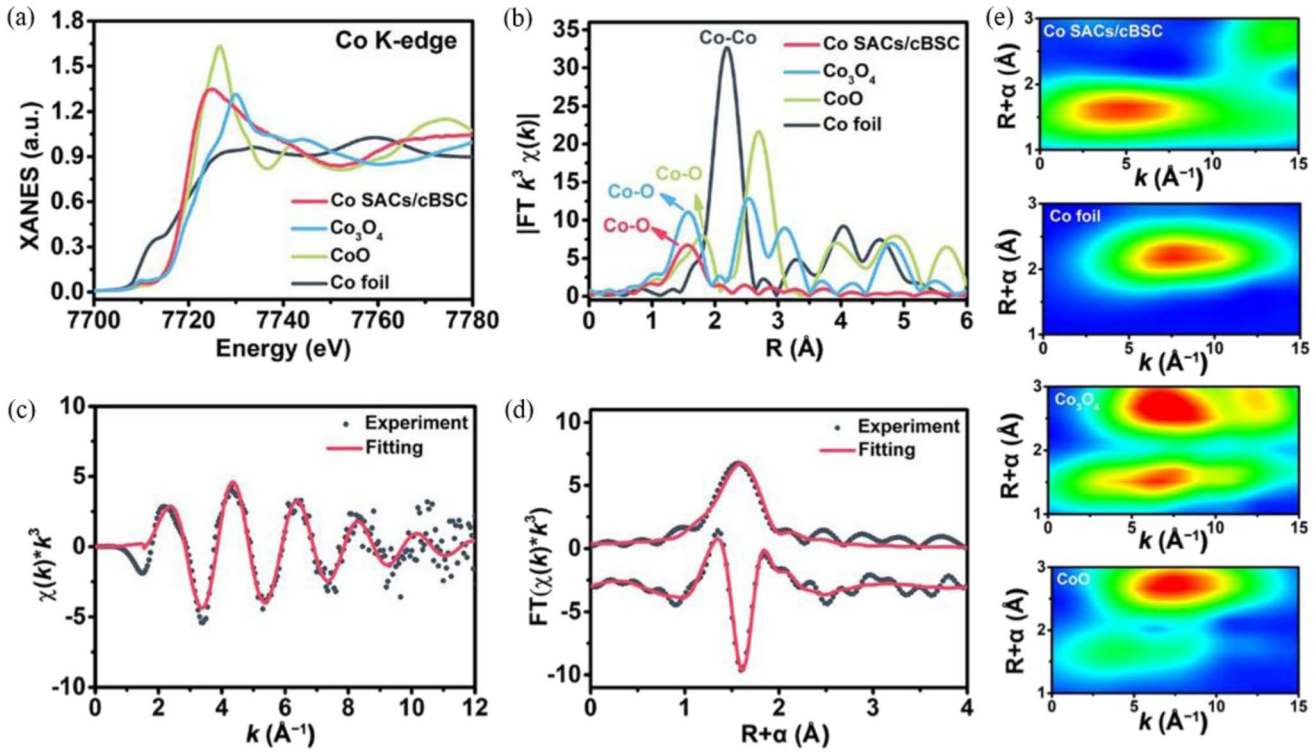


Fig. 6 (a) Normalized XANES spectra, (b) first-shell fitting of EXAFS curves, (c) Co K-edge EXAFS (points) and the curve-fit (line) spectra, (d) EXAFS fitting curves of Co SACs/carriers in *R* space, and (e) wavelet-transform plots of corresponding samples, reproduced with permission.[78] Copyright 2024, Wiley-VCH.

in $I_2$@PFC-72-Co nanomaterials *via* XPS analysis, ascribing the peaks at 400.4 eV and 399.5 eV in the high-resolution N 1s spectrum to pyrrole C–N and N–Co, respectively (Fig. 7a). In addition, the dual peaks at 777.2 eV and 780.6 eV along with the satellite peak at 785.5 eV were assigned to Co $2p_{3/2}$, while the main peak at 795.7 eV and the satellite peak at 801.1 eV were associated with Co $2p_{1/2}$ (Fig. 7b). These results suggest the formation of Co SACs in the composite materials. In Fig. 7c, the energy space of Co $2p_{3/2}$ and Co $2p_{1/2}$ was 15.8 eV, revealing that the valence state of Co was +2. In another study, the XPS survey spectrum (Fig. 7d) confirmed the presence of C, N, O, and Fe peaks in the prepared materials.[80] In the high-resolution N 1s spectrum (Fig. 7e), the peaks at 398.3 eV, 399.5 eV, 400.7 eV, and 403 eV were related to the pyridinic-N and Fe–N bond, pyrrolic-N, graphite-N, and oxidized-like-N species, respectively. The high-resolution Fe 2p spectrum (Fig. 7f) displayed two peaks at 712.32 eV and 725.65 eV, corresponding to Fe $2p_{3/2}$ and Fe $2p_{1/2}$, respectively. Moreover, the distance between Fe $2p_{3/2}$ and Fe $2p_{1/2}$ was 13.3 eV, indicating the presence of $Fe^{3+}$. In particular, no peaks were observed for zero valent metallic Fe in Fig. 7f, indicating the absence of metallic agglomeration and further revealing the successful preparation of Fe SACs. Overall, XPS is a facile and quick technique, making it a promising tool for the characterization of SACs. Nevertheless, it also has some limitations: low SAC loading leads to low signal intensity; characterization focuses only on the surfaces; and the presence of SACs cannot be directly confirmed.

### 4.4 Other characterization techniques

Scanning tunneling microscopy (STM) is another powerful technique for investigating the electronic properties and morphology of SACs. *Via* quantum tunneling, STM can achieve atomic-scale resolution on conductive surfaces and can map the local electronic density of states of SACs, providing insights into the interactions between substrates and SACs.[81] As an example, Deng *et al.*[82] observed that the Fe center appeared as a bright spot, and the neighboring C and N atoms also appeared brighter than the carbon atoms situated further away in Fe–$N_4$/graphene ($FeN_4$/GN-2.7; Fig. 7g). The STM simulation results (Fig. 7h) confirmed that the Fe center was embedded in the graphene lattice and significantly modified the density states of adjacent atoms. As discussed previously, TEM has limitations in distinguishing two metal atoms, whereas STM can identify different metal atoms due to the topographical and electronic differences between two metals, resulting in the single metal site appearing as bright protrusions or dark depressions on the substrate.[83] For instance, Giannakakis *et al.*[84] proved that Rh atoms were present on the Cu(111) surface through STM imaging (Fig. 7i) and the corresponding simulated STM image (Fig. 7j). However, the broader application of STM for the characterization of SACs is limited due to the stringent requirements including highly conductive materials and smooth surfaces and ultra-high vacuum conditions, which often do not represent the conditions of actual catalytic reactions.[85] Therefore, STM is usually regarded

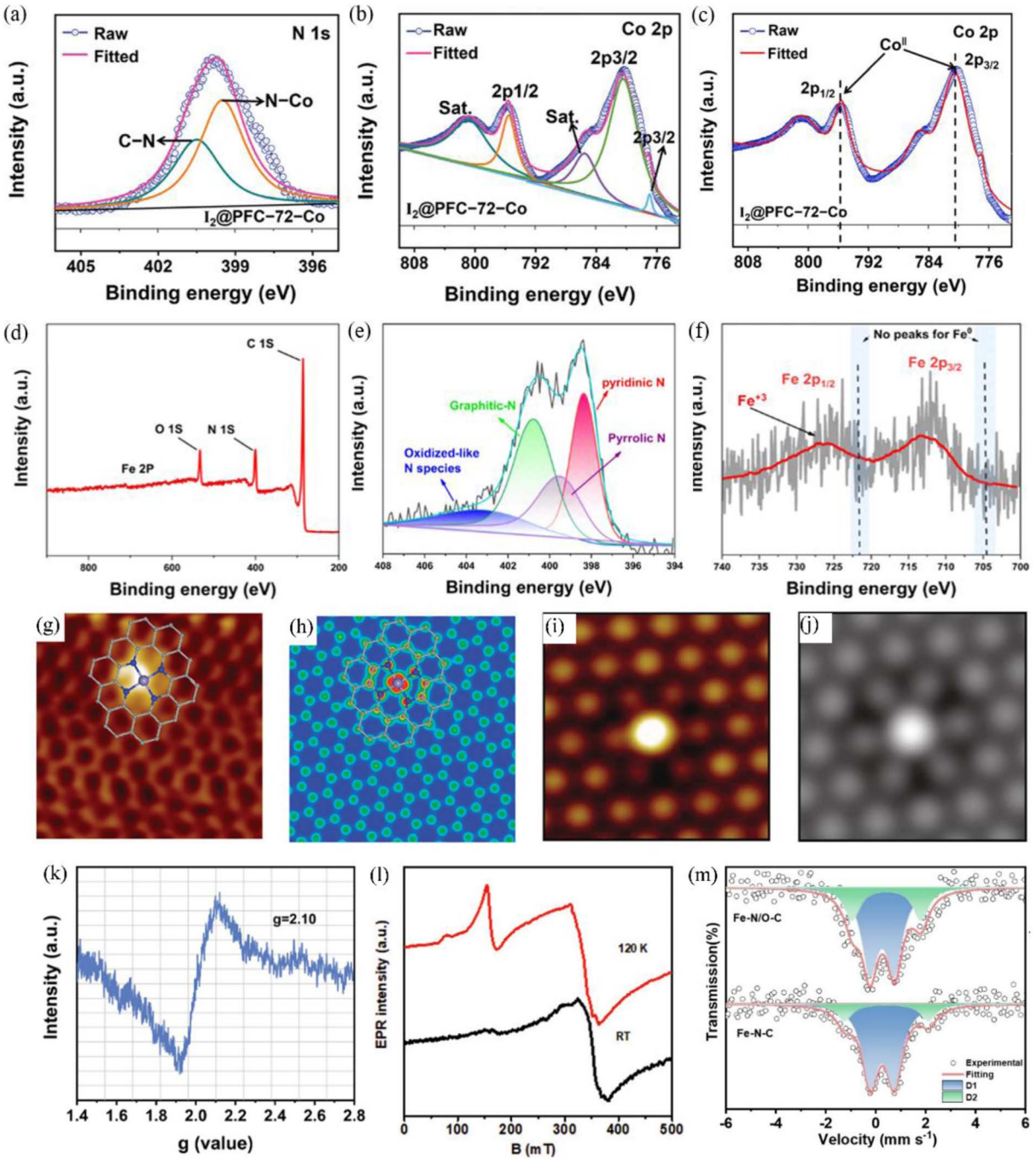


Fig. 7 (a) High-resolution N 1s and (b and c) Co 2p XPS spectra of $I_2$@PFC-72-Co (iodine/PFC-72-Co hydrogen-bonded cobalt porphyrin framework), reproduced with permission.[79] Copyright 2024, Wiley-VCH. (d) XPS survey spectrum and high-resolution (e) N 1s and (f) Fe 2p XPS spectra of $Fe_{SAC}$-N-C (Fe SAC-nitrogen-doped carbon nanosheets), reproduced with permission.[80] Copyright 2023, American Chemical Society. (g and h) Experimental and simulated STM images of $FeN_4$/GN-2.7, reproduced with permission.[82] Copyright 2015, American Association for the Advancement of Science. (i and j) Experimental and simulated STM images of Rh atoms in Cu (111), reproduced with permission.[84] Copyright 2021, American Association for the Advancement of Science. (k) EPR spectra of Fe SACs/nitrogen-doped carbon support, reproduced with permission.[88] Copyright 2023, Wiley-VCH. (l) EPR spectra of FeSA-NSC, reproduced with permission.[89] Copyright 2022, Wiley-VCH. (m) Fe Mössbauer spectra of Fe SACs with the co-coordination of N and O (Fe–N/O–C) and Fe SACs with the co-coordination of N (Fe–N–C), reproduced with permission.[91] Copyright 2024, Wiley-VCH.

as a complementary technique rather than standalone evidence for confirming SACs.

Electron paramagnetic resonance (EPR) is a highly sensitive technique that can provide valuable information on SACs, including the electronic and local coordination environment, metal oxidation state, and interactions between SACs and supporting materials.[86] Notably, EPR requires sufficient magnetic response from the samples and is thus usually used in

 

combination with other characterization techniques. EPR can also be carried out under relatively high temperature (≤873 K) and pressure (≤20 bar) conditions.[87] As shown in Fig. 7k, the *g* value was calculated to be 2.10, corresponding to the coordinatively unsaturated Fe SACs/nitrogen-doped carbon support.[88] In another study, Li *et al.*[89] observed that the *g* values of Fe SACs/sulfur-and-nitrogen-codoped carbon matrix ($Fe_{SA}$-NSC) were 2.005 and 2.026 at room temperature and 120 K, respectively (Fig. 7l), which was attributed to the unpaired electron in the $e_g$ orbital of Fe SACs. The EPR results, combined with the XAS and XPS results, confirmed the successful preparation of Fe SACs and the +1 valence of Fe.

Mössbauer spectroscopy is another powerful technique for elucidating the chemical state, spin state, and coordination environments of materials through recoilless nuclear resonance emission and absorption of γ-rays. It is particularly useful for the characterization of materials containing Fe[90] and can also be applied to distinguish Fe SACs and Fe-based oxides. As illustrated in Fig. 7m, the absence of α-Fe and γ-Fe characteristic peaks in both Fe–N/O–C and Fe–N–C suggests that the pure metal phase was absent in the samples.[91] The Mössbauer spectra of prepared materials were fitted with two doublets, named D1 and D2, which were assigned to $Fe(II)N_4$ (low spin) and $Fe(II)N_4$ (medium spin), respectively. In addition, the D1 peak area increased and the D2 peak area decreased in Fe–N–C relative to Fe–N/O–C, indicating that the coordinated O atom resulted in the transition of Fe SACs from a low spin state to a medium spin state.

At present, *in situ* techniques are essential for investigating the underlying mechanisms of SACs during reactions. It would be highly valuable to monitor the electronic structures, coordination environments, and valence states of SACs in real-time. These *in situ* techniques (*e.g.*, TEM, XAS, XPS, and X-ray diffraction (XRD)) have been comprehensively summarized and discussed in different research areas, such as photocatalysis,[92] the oxygen evolution reaction,[93] batteries,[94] nitrate electroreduction,[95] and electrochemical $CO_2$ reduction.[96] However, *in situ* characterization of SACs remains challenging due to various inherent limitations of each technique (as discussed above). The integration of multiple characterization techniques and the combination of theoretical calculations (*e.g.*, density functional theory (DFT)) are promising to investigate the properties of SACs.

# 5. Electrochemical nitrate reduction by non-noble metal single atoms

The properties of non-noble metal single atoms play key roles in electrochemical nitrate reduction. In this section, the performance of electrochemical nitrate reduction by different non-noble metal single atoms (*e.g.* Fe, Cu, Ni, and Co) is evaluated in terms of key performance parameters, including $NH_3$ yield, faradaic efficiency, selectivity, stability, and economic and environmental indicators. In addition, the influences of operation conditions, including electrolyte type, overpotential, temperature, and current density, are critically examined.

## 5.1 Fe single atoms

Among the various candidates, Fe-based single atoms have been widely explored for electrochemical nitrate reduction because of their excellent catalytic properties. As an example, Wu *et al.*[97] prepared Fe SACs ($Fe–N_4$) with a high faradaic efficiency of 75% and $NH_3$ yield of 7.83 mg $h^{-1}$ $cm^{-2}$ for electrochemical ammonia production. In another example, Li *et al.*[98] observed that the prepared Fe SACs coordinated with nitrogen of carbon materials (Fe-PPy SACs and $Fe–N_4$), displaying a high $NH_3$ yield of 2.75 mg $h^{-1}$ $cm^{-2}$ with nearly 100% faradaic efficiency during the electrosynthesis of ammonia from nitrate. DFT calculations elucidated that $NO_3^-$ preferentially adsorbed on the Fe SACs *via* an end-on configuration through a single O atom, whereas adsorption on Fe nanoparticles occurred *via* a side-on mode through two O atoms (Fig. 8a and b). The partial density of states of Fe-PPy SACs and Fe nanoparticles indicates that the adsorbed $NO_3^-$ on Fe-PPy SACs was more active due to the obvious hybridization between O p and Fe d and significant overlap of electron densities in antibonding orbitals (Fig. 8c). The Gibbs free energy diagram suggests that $NH_3$ generation involved a nine-step pathway, and the free energy difference ($\Delta G$) of $NO_3^-$ adsorption on Fe SACs was more negative than that of $H_2O$ adsorption (Fig. 8d), indicating that almost all the active sites of Fe SACs were occupied by $NO_3^-$. Additionally, the $\Delta G$ of *H desorption (rate-limiting step for the HER) by Fe-PPy SACs was higher than that for Fe nanoparticles (1.42 eV > 0.81 eV), suggesting that Fe SACs promoted the formation of $NH_3$ while suppressing the HER.

Furthermore, the coordination environments of SACs are decisive factors in electrochemical nitrate reduction, as they can change the electronic structures of materials and further affect the catalytic performance. For instance, Liu *et al.*[99] synthesized different Fe-based SACs, including $OH–Fe–N_4$, $Fe–N_3$, and $Fe–N_4$, at different pyrolysis temperatures of 800 °C, 900 °C, and 1000 °C, respectively. $Fe_1$/NC-900 ($Fe–N_3$) displayed the highest $NH_3$ yield and faradaic efficiency (Fig. 8e–f), which was mainly attributed to the abundant lone pair electrons and the enhanced charge transfer and reduced energy barrier during the nitrate reduction process. In addition, $Fe_1$/NC-900 displayed the highest $NH_3$ yield at −0.9 V *vs.* RHE, while the faradaic efficiency was decreased compared to −0.7 V *vs.* RHE, which is related to the complete reaction of the HER. Xu *et al.*[100] also reported that the Fe SACs coordinated with nitrogen and phosphorus on hollow carbon exhibited an outstanding $NH_3$ production yield and faradaic efficiency for electrocatalytic nitrate reduction. In Fig. 8g, synchrotron radiation Fourier transform infrared (SR-FTIR) spectra demonstrate that the peak intensity of $NO_3^-$ increased with applied potential, indicating the continuous reduction of $NO_3^-$. Fig. 8h proves that the key intermediates, including $\sigma$(N–H), $*NH_4^+$, and $*–O_2N$, were generated during $NH_3$ production. The experimental results and DFT calculations prove that P atoms break the local charge symmetry of Fe SACs and further promote the adsorption of nitrate and key reactions for nitrate reduction. Additionally, Zhang *et al.*[101] proved that Fe SACs with $FeN_2O_2$ coordination displayed higher electrochemical nitrate reduction efficiency

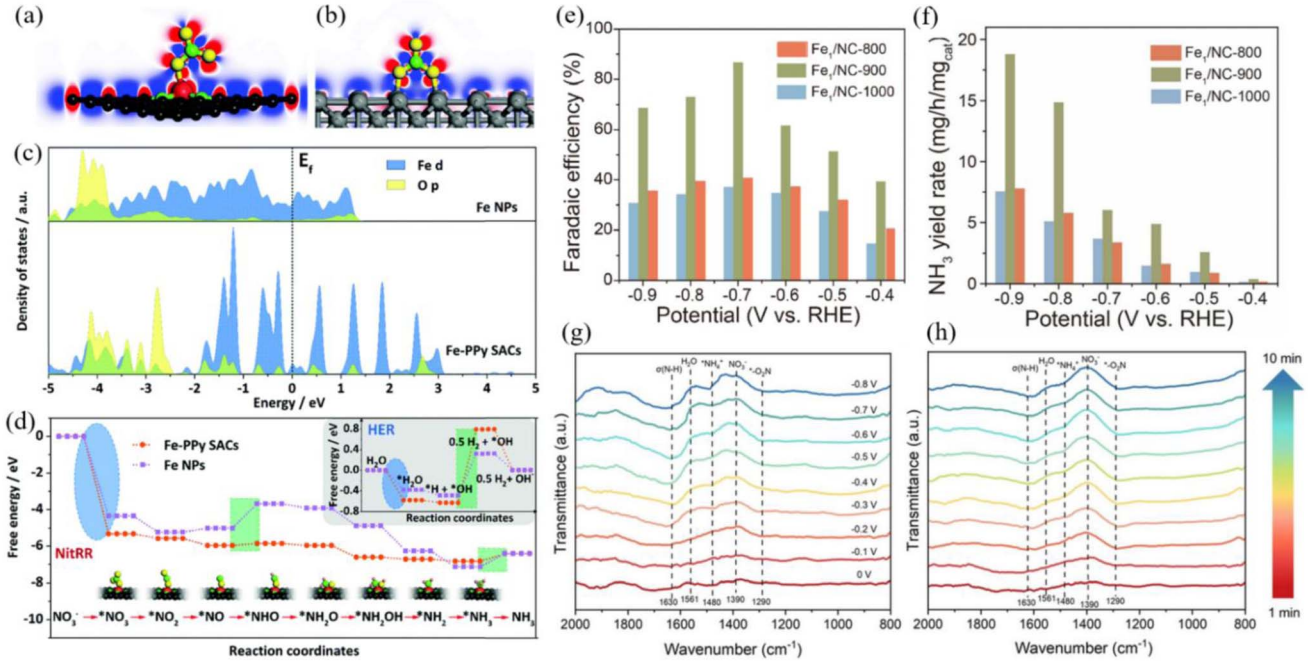


Fig. 8 (a) DFT calculations of $NO_3^-$ adsorption by Fe-PPy SACs and (b) Fe nanoparticles, (c) the partial density of states of Fe-PPy SACs and Fe nanoparticles, and (d) Gibbs free-energy of nitrate reduction and water dissociation, reproduced with permission.[98] Copyright 2021, The Royal Society of Chemistry. (e) Faradaic efficiency and (f) $NH_3$ production yield of Fe SACs at different potentials, reproduced with permission.[99] Copyright 2023, Elsevier. (g) SR-FTIR spectra at different potentials, and (h) time-dependent SR-FTIR spectra at a potential of −0.4 V *vs.* RHE, reproduced with permission.[100] Copyright 2023, Wiley-VCH.

compared to Fe SACs with $FeN_4$ coordination, which was mainly attributed to the $FeN_2O_2$ structure presenting higher conductivity and excellent $NH_3$ selectivity and reducing rate-limiting steps and inhibiting the formation of some byproducts (*e.g.*, $NO_2^-$).

In addition to carbon-rich materials, another class of novel materials, namely, MXenes, has also been applied for the immobilization of Fe SACs. Generally, MXenes are prepared by etching MAX ceramics, and the formula is $M_{n+1}AX_n$, where M is an early transition metal element and A and X refer to an element of group IIIA-VA and C and/or N, respectively. MXenes, as two-dimensional materials, have attracted considerable attention due to their layered structure, high conductivity, and adjustable surface properties.[102] Ren *et al.*[103] observed that Fe SACs/$Ti_3C_2T_x$ MXene demonstrated a higher $NH_3$ faradaic efficiency and selectivity (83%, 99%) compared with Fe nanoparticles/MXene (69%, 81%) and MXene (33%, 52%) during electrocatalytic nitrate to ammonia conversion. They also proved that the high performance of Fe SACs/$Ti_3C_2T_x$ MXene was related to the inhibition of the HER and reduced activation energy for the rate-limiting steps. Moreover, metal oxides have also been considered as supports for SACs. For instance, Murphy *et al.*[104] reported that the synthesized $Fe_2O_3$ nanoparticles/Fe–N–C (Fe SACs-N-C) composite demonstrated a high $NH_3$ yield of 9 mmol $h^{-1}$ $cm^{-2}$ and an excellent faradaic efficiency of around 100% (at −1.2 V *vs.* RHE) for electrochemical nitrate reduction. In addition to the high performance of Fe–N–C, it was also proven that the pre-reduction activation step (−1.5 V *vs.* RHE for 90 s) was crucial to produce $NH_3$ due to the reduction of $Fe^{3+}$($Fe_2O_3$) to the highly active $Fe^0$. Wang *et al.*[105] also prepared Fe SAC doped $TiO_2$ composites with an excellent faradaic efficiency of 92.3% and ammonia yield of 137 mg $h^{-1}$ $mg_{cat}^{-1}$. They observed that the Fe SAC doping introduced abundant oxygen vacancies in the composites, which promoted active sites for the adsorption and reduction of nitrate. The synergistic effects between oxygen vacancies and Fe SACs resulted in high electrocatalytic nitrate reduction efficiency.

### 5.2 Cu single atoms

Inspired by Cu-containing nitrate reductases in nature, Cu SACs have been extensively studied for electrochemical nitrate reduction to ammonia due to their outstanding catalytic performance, high stability, and superior selectivity.[106] For instance, Zhao *et al.*[107] prepared Cu SACs exhibiting a high $NH_3$ production efficiency of 2.6 mg $cm^{-1}$ $h^{-1}$ and high faradaic efficiency (87%) and selectivity (94%) for electrochemical nitrate reduction. The experimental results and DFT calculations reveal that the $CuN_4$ active sites promoted the adsorption and activation of nitrate, resulting in the selective production of $NH_3$ with a downhill free energy pathway. Yin *et al.*[108] also observed that Cu SACs demonstrated a higher $NH_3$ reduction and faradaic efficiency compared with the prepared Mn SACs, Ni SACs, and Mo SACs. This is mainly due to the hybridization between Cu SACs and O being greater compared with that of other prepared SACs, leading to faster electron transfer between nitrate and Cu SACs. The $CuN_4$ coordination environments

 

could also inhibit the side reactions (*e.g.*, generation of $N_2$ and $N_2O$) and enhance the production of $NH_3$.

In order to further improve $NH_3$ production efficiency during electrochemical nitrate reduction, the combination of Cu SACs with other catalysts has been reported to be an effective strategy. As an example, Zuo *et al.*[109] prepared porous N-doped/Cu SACs/La-based nanoparticles (p-CNCuLa-m) through systematic enhancements, including ultraviolet irradiation, confined synthesis, and microwave treatment. As illustrated in Fig. 9a–d, the broad peaks at around 280 $cm^{-1}$ and 693.4 $cm^{-1}$ were assigned to La–O (La-$ON_x$) and Cu–O (Cu-$ON_x$), respectively. Also, *p*-CNCuLa-m demonstrated a stronger La–O peak and weaker Cu–O peak compared to *p*-CNCuLa (without microwave treatment), indicating that more La-based atoms were exposed on the surface after microwave irradiation. Mechanistic analysis proves that Cu SACs exhibited excellent electroactivity for the reduction of nitrate, and La-based nanoparticles as proton donors improved electron transfer efficiency. Synergies between Cu SACs and La-based clusters reduced the energy barriers and promoted the production of $NH_3$. In another study, Liu *et al.*[110] prepared Cu SACs with adjacent $Co_3O_4$ nanosheets, resulting in excellent electroreduction efficiency of nitrate (114 mg $h^{-1}$ $cm^{-2}$). They also developed a Raman cell for *in situ* detection of the intermediates during electroreduction (Fig. 9e), with the distance between the laser and electrode surface adjustable mechanically. As shown in Fig. 9f–g, based on the peak at around 810 $cm^{-1}$ ascribed to the $NO_2^-$ intermediate, Cu SACs/$Co_3O_4$ demonstrated a lower $NO_2^-$ intensity compared to Cu SACs, indicating that $Co_3O_4$ could regulate the adsorption of $NO_2^-$ to further boost the electroreduction of nitrate to $NH_3$.

As discussed above, the coordination environments of SACs play key roles in the electrochemical reduction of nitrate by modulating the electronic structure of the active sites and thus governing catalytic performance. This was further confirmed by Cu SACs in the electrocatalytic production of $NH_3$. As shown in Fig. 9h, Liu *et al.*[111] proved that Cu-pyridinic-$N_4$ could significantly reduce the energy barriers for converting *NO to *NHO (0.51 eV to 0.07 eV) and inhibit the HER compared to Cu-pyrrolic-$N_4$ for the electroreduction of nitrate, resulting in an excellent Faraday efficiency of 94% and $NH_3$ production efficiency (130 mg $h^{-1}$ $mg_{cat}^{-1}$). Cheng *et al.*[112] also reported that Cu-*cis*-$N_2O_2$ (two N atoms on the same side) displayed higher $NH_3$ production efficiency compared with Cu-*trans*-$N_2O_2$ (two N atoms on the opposite side) and Cu–$N_4$, which was mainly because Cu-*cis*-$N_2O_2$ with low coordination symmetry provided more active sites for the adsorption of nitrate and reduced the energy barrier for the generation of the key intermediate (*ONH). As another example, Yang *et al.*[113] observed *via*

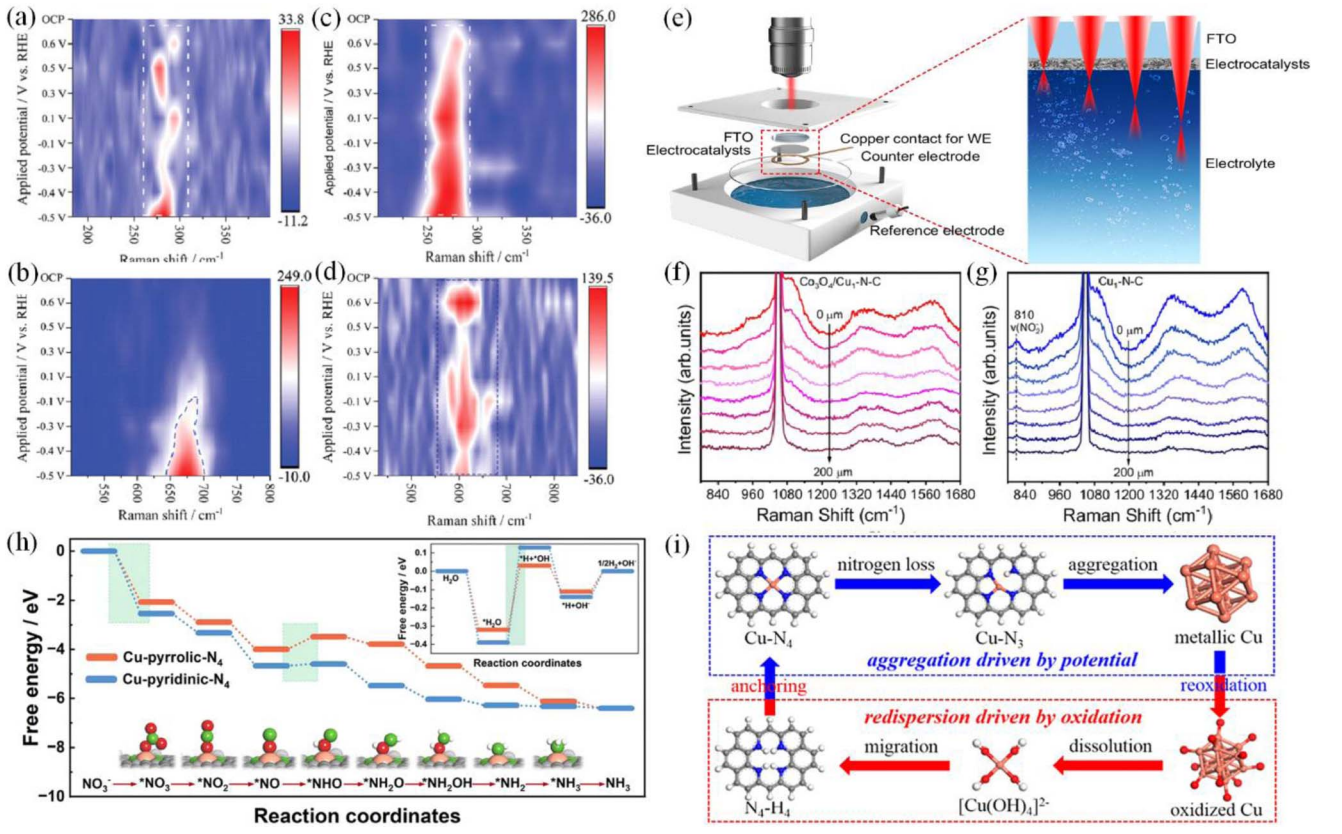


Fig. 9 (a and b) *In situ* Raman spectra of electrochemical nitrate reduction by *p*-CNCuLa and (c and d) *p*-CNCuLa-m, reproduced with permission.[109] Copyright 2025, Wiley-VCH. (e) Schematic diagram of the designed Raman cell. *In situ* Raman spectra of (f) Cu SACs/$Co_3O_4$ and (g) Cu SACs, reproduced with permission.[110] Copyright 2024, Springer Nature. (h) Gibbs free energy diagram of electroreduction of nitrate and water dissociation by Cu-pyridinic-$N_4$ and Cu-pyrrolic-$N_4$, reproduced with permission.[111] Copyright 2024, Elsevier. (i) Transformation between Cu–$N_4$ structures and $Cu^0$ nanoparticles, reproduced with permission.[113] Copyright 2022, American Chemical Society.

*operando* XAS analysis that the synthesized Cu–$N_4$ structures were subsequently transformed into Cu–$N_3$ and $Cu^0$ nanoparticles when the applied potential changed from 0 V to −1 V *vs.* RHE (Fig. 9i). They also proved that the $Cu^0$ nanoparticles were active sites for the electrochemical nitrate reduction and the transitions between Cu–$N_4$ structures and $Cu^0$ nanoparticles were driven by applied potential and oxidation environments. Interesting studies have also been reported for boosting $NH_3$ production during electrochemical nitrate reduction. For instance, Xu *et al.*[114] synthesized an ultrasmall and uniform Cu SACs/Ce-UiO-66 catalyst (4 nm) through the confined effects of Ce-UiO-66 to prevent excessive aggregation of Cu SACs. The size effects and host–guest interactions between Cu SACs and Ce-UiO-66 promoted nitrate activation and reduced energy barriers, resulting in an outstanding $NH_3$ production efficiency (55 mg $h^{-1}$ $mg_{Cu}^{-1}$).

### 5.3 Ni single atoms

Ni SACs are also popular for electrochemical reduction of nitrate due to their relatively high catalytic performance and selectivity. For instance, Ajmal *et al.*[115] reported that the synthesized Ni SACs/boron, nitrogen-doped graphene demonstrated a high $NH_3$ production rate of 168 μg $h^{-1}$ $cm^{-2}$ and faradaic efficiency of 95%. Fig. 10a and b show the high catalytic efficiency at different nitrate concentrations (50–1000 mM) and excellent durability after five cycles, which was related to the superior catalytic activities of Ni SACs and the improved nitrate adsorption by boron doping. In addition, the combination of nanoparticles with Ni SACs has been reported to further improve the efficiency of electrochemical nitrate reduction. Zhao *et al.*[116] proved that the high nitrate reduction efficiency by Ni SACs/Ni nanoparticles/boron, carbon, nitrogen matrix was related to the excellent catalytic performance of Ni SACs and Ni nanoparticles, while the boron, carbon, nitrogen matrix also reduced the energy barriers to produce $NH_3$. In a similar study, Xi *et al.*[117] confirmed that Ni nanoparticles could not only regulate the electron-deficient state of Ni SACs and enrich the nitrate near the catalysts but also promote the formation of $NO_3^*$ to further improve the electrochemical nitrate reduction efficiency. Moreover, single-atom alloys (SAAs), which are defined as metal atoms atomically dispersed on the surface of another metal host, have emerged as promising candidates for heterogeneous catalysis.[118] SAAs typically display properties of both alloys and SACs, with well-defined active sites, unique electronic structures, and ultrahigh atom utilization of SAAs leading to excellent catalytic performance.[119] There have been interesting reports on the application of SAAs for electrochemical nitrate reduction. For instance, Cai *et al.*[120] synthesized a Ni SAC-alloyed Cu catalyst through *in situ* electrochemical reduction (Fig. 10c), and the resulting catalysts demonstrated an excellent faradaic efficiency of near 100% and $NH_3$ production rate of 327 μmol $h^{-1}$ $cm^{-2}$ for electrochemical nitrate conversion. They also observed that the Ni SAC-alloyed Cu catalyst regulated nitrate reduction by improving the interaction between Ni SACs and intermediates (*e.g.*, NOOH*), which reduced the potential of the reaction and contributed to the ultrahigh efficiency of electrochemical nitrate reduction.

### 5.4 Other non-noble metal single atoms

Other non-noble metal SACs, including Mn-, Zn- and Bi-based systems, have been investigated for electrochemical nitrate reduction. Although these SACs are not as widely used as Fe, Cu,

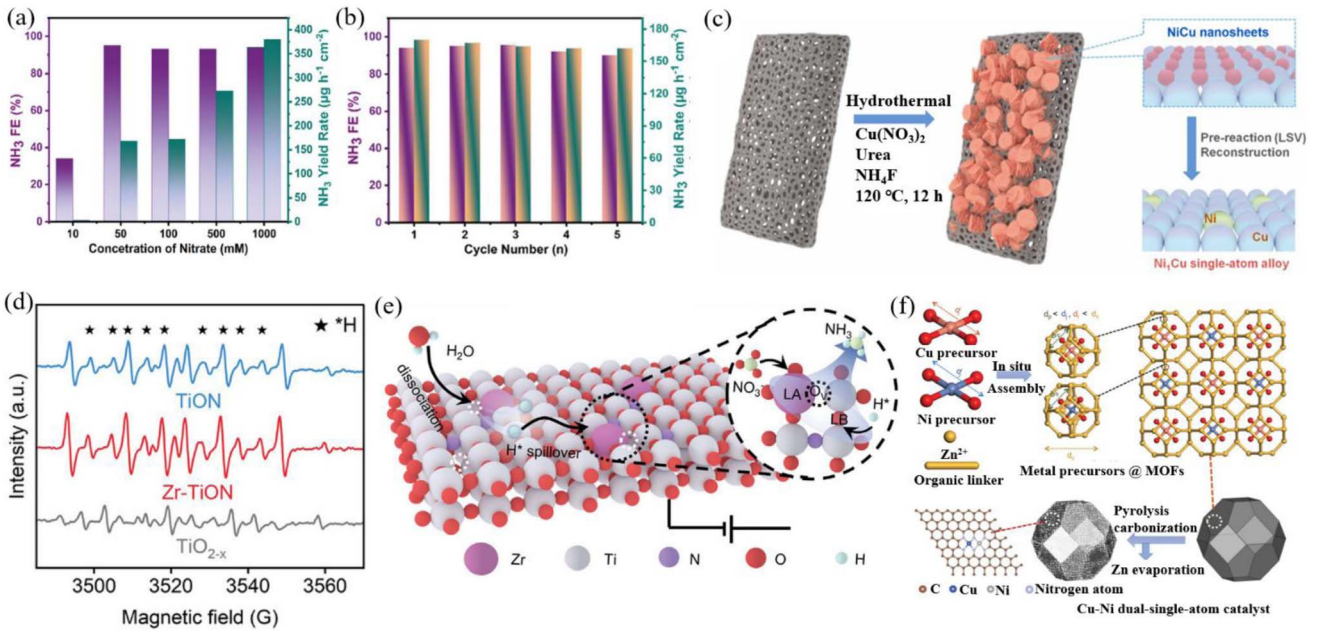


Fig. 10 (a) Faradaic efficiency and $NH_3$ yield rate at various $NO_3^-$ concentrations, and (b) consecutive recycling test of Ni SACs/boron and nitrogen-doped graphene, reproduced with permission.[115] Copyright 2024, Wiley-VCH. (c) Schematic illustration of the Ni SAC-alloyed Cu catalyst synthesis process, reproduced with permission.[120] Copyright 2022, Elsevier. (d) EPR spectra of the prepared catalysts, and (e) schematic illustration of the electrochemical nitrate reduction process by Zr-TiON, reproduced with permission.[123] Copyright 2024, Wiley-VCH. (f) Schematic illustration of the Cu–Ni dual single-atom catalyst preparation process, reproduced with permission.[127] Copyright 2023, Wiley-VCH.

Table 1 Summary of non-noble metal single-atom catalysts for electrochemical nitrate reduction. H-type reactor cells and simulated wastewater were used in all cases

| Catalysts | Electrolytes/(pHs) | Potentials (V *vs.* RHE) | Current density (mA $cm^{-2}$) | $NH_3$ yield/ (reaction time) | Faraday efficiencies | Ammonia quantification methods | Main mechanisms | Ref. |
|---|---|---|---|---|---|---|---|---|
| Cu(I)-$N_3C_1$ | 50 mM $Na_2SO_4$/100 ppm $NaNO_3$ (neutral pH) | −0.64 | ∼−10 | 5466 mmol g $Cu^{-1}$ $h^{-1}$ (6 h) | 52% | Isotope verification | Cu(I)-$N_3C_1$ reduced the activation energy of the rate-limiting steps for the production of $NH_3$ | 129 |
| Cu SAC-based aerogel | 0.1 M $Na_2SO_4$/100 ppm $NaNO_3$ (pH unadjusted) | −0.9 | ∼−5.5 (−1.5v) | 330 μg $h^{-1}$ $cm^{-2}$ (0.5 h) | 87% | UV-vis spectroscopy | Cu–$N_2$ active site decreased the energy barriers to promote $NH_3$ production | 130 |
| Cu SACs/B doped CN | 0.1 M KOH/100 mM $NO_3^-$ (pH unadjusted) | −0.6 | ∼−40 | 3358 μg $h^{-1}$ $cm^{-2}$ (1 h) | 97% | Isotope verification | The B element enhanced the catalytic activity for nitrate, and this process was exothermic | 131 |
| Cu SACs/iron oxide/nanoscale zero-valent iron | 0.1 M $K_2SO_4$/50 ppm $NO_3^-$ (pH unadjusted) | −1.3 | — | 1980 μg $h^{-1}$ $cm^{-2}$ (3h) | 95.4% | Isotope verification | Fe active sites improved the $NO_3^-$ adsorption capacity, and Cu sites enhanced the water activation; this synergistic effect decreased the energy barriers for nitrate reduction | 132 |
| Single-atom Bi alloyed Pd metallene | 1 M KOH/100 mM $NO_3^-$ (pH unadjusted) | −0.6 | ∼−400 | 33.8 mg $h^{-1}$ $cm^{-2}$ (1 h) | Near 100% | Isotope verification | The catalysts decreased the energy barrier of the potential-determining step and enhanced protonation energetics | 133 |
| Fe SACs/FeP nanoparticles | 0.05 m $H_2SO_4$/0.5 m $KNO_3$ (pH 1.2) | −1.0 | ∼−100 | 36.2 mg $h^{-1}mg_{cat}^{-1}$ (0.5 h) | 95.6% | Isotope verification | The unique charge redistribution and optimized electronic structure of catalysts strengthened intermediate adsorption and catalytic activity | 17 |
| Dual single-atom molybdenum and iron alloy | KOH/$KNO_3$ (pH unadjusted) | −0.7 | ∼−200 | 13.4 mol $g_{cat.}^{-1}$ $h^{-1}$ (1 h) | 94.6% | Isotope verification | Mo and Fe atoms altered the interfacial water structure to restrain the competing HER and regulated the electronic structure | 134 |
| Fe SAC/NC | 1 M KOH/1000 μg $mL^{-1}$ $KNO_3$ (pH unadjusted) | −0.8 | — | 22.5 mg $h^{-1}mg_{cat}^{-1}$ (2 h) | 98.2% | Isotope verification | Pyrrole-$N_3$-Fe reduced the energy barrier for the transition of *NO to *NHO, thereby improving the production activity and selectivity of ammonia | 135 |
| Boron-doped Fe SAC | 1 M KOH/0.5 M $KNO_3$ (pH unadjusted) | −0.3 | ∼−25 | 2.17 mg $h^{-1}$ $cm^{-2}$ (1.5 h) | 97.48% | Isotope verification | The incorporation of B regulated the intermediate adsorption on SACs, thereby enhancing nitrate reduction efficiency | 136 |

Table 1 (*Contd.*)

| Catalysts | Electrolytes/(pHs) | Potentials (V *vs.* RHE) | Current density (mA $cm^{-2}$) | $NH_3$ yield/ (reaction time) | Faraday efficiencies | Ammonia quantification methods | Main mechanisms | Ref. |
|---|---|---|---|---|---|---|---|---|
| Cu–$N_1O_2$ SACs | 0.1 M KOH/0.01 M $KNO_3$ (pH 13) | −0.6 | ∼−290 | 3120 μg $h^{-1}$ $cm^{-2}$ (1 h) | 96.5% | Isotope verification | The catalysts facilitated the accumulation of $NO_3^-$ and the selective adsorption of $*NO_2$ on Cu–$N_1O_2$ SACs | 137 |
| $Fe_{SA}$-N-C/Fe nanoparticles | 0.5 M $K_2SO_4$/0.1 M $KNO_3$ (pH unadjusted) | −0.9 | — | 4042 μg $h^{-1}$ $mg_{cat}^{-1}$ (—) | 95.5% (−0.85V) | Isotope verification | Fe SACs adsorbed and activated $NO_3^-$ to form *NO intermediates, while $Fe_{NP}$ accelerated water dissociation to provide more *H | 138 |
| Fe SACs@$MoS_2$/carbon fiber cloth | 1M KOH/0.6 M $KNO_3$ (pH unadjusted) | −0.73 | ∼−350 | 28.59 mg $h^{-1}$ $cm^{-2}$ (1 h) | 96.65% | UV-vis spectroscopy | The synergistic tandem effect of atomic Fe and surrounding Mo edge sites enhanced electron transfer, increased nitrate adsorption, and decreased free energy of ammonia desorption | 139 |

and Ni SACs, excellent electrochemical nitrate reduction efficiencies have been reported. As an example, Zhang *et al.*[121] reported that the synthesized Mn SACs exhibited outstanding electrochemical nitrate reduction performance with an $NH_3$ yield of 1476 μg $h^{-1}$ $cm^{-2}$ and a faradaic efficiency of 89%. They also proved that Mn-$(O–C_2)_4$ as predominant active sites not only improved adsorption and activation efficiency of nitrate but also restricted the HER, resulting in high generation efficiency and selectivity of $NH_3$. As another example, Zhao *et al.*[122] prepared Zn SACs/N-doped carbon through a combined dissolution-vaporization-pyrolysis process. The catalysts achieved a high nitrate conversion efficiency of 97% and a high faradaic efficiency of 95%, which were related to the reduced energy barriers for the rate-determining step during electrochemical nitrate reduction. In addition, Yang *et al.*[123] prepared Zr SACs/N-doped $TiO_{2-x}$(Zr–TiON) with abundant oxygen vacancies for efficient electrochemical nitrate reduction to ammonia. As shown in Fig. 10d, both Zr–TiON and TiON displayed strong *H signals, indicating that nitrogen doping was beneficial for hydrolysis dissociation and further enhanced the generation of active hydrogen. Fig. 10e shows that Zr SACs and surrounding oxygen atoms served as Lewis acidic and Lewis basic sites, respectively, facilitating the adsorption and activation of nitrate and *H, thus improving electrochemical nitrate reduction activity. In addition, Bi-based catalysts have been demonstrated to be promising candidates for electrochemical nitrate reduction due to the relatively low catalytic performance in the HER.[124] For instance, Zhang *et al.*[125] observed that the prepared Bi SACs ($BiN_2C_2$) displayed a remarkable faradaic efficiency of 89% and $NH_3$ yield rate of 1.38 mg $h^{-1}$ $mg_{cat}^{-1}$ during electrochemical nitrate reduction to ammonia, which were attributed to the abundant active site ($BiN_2C_2$) and low charge of Bi centers being conducive to stabilizing the hydrogenated intermediates.

Recently, dual single-atom catalysts have been reported to demonstrate some advantages compared to SACs, such as optimizing reaction thermodynamics, enhancing reaction kinetics, and regulating electronic interactions.[126] Different dual single-atom catalysts have also been explored for electrochemical nitrate reduction. As illustrated in Fig. 10f, Wang *et al.*[127] prepared Cu–Ni dual single-atom catalysts/N-doped carbon through pyrolysis. The high $NH_3$ faradaic efficiency of 97% during electrochemical nitrate reduction was tied to the Cu–Ni dual active sites. Specifically, the strong orbital hybridizations accelerated the electron transfer between catalysts and nitrate, and dual single-atom active sites reduced rate-limiting step barriers and inhibited side reactions (*e.g.*, the HER and $N_2$ generation). As another example, Wan *et al.*[128] observed that Fe–Mo dual single-atom catalysts exhibited a high $NH_3$ yield of 13.56 mg $cm^{-2}$ $h^{-1}$ and a faradaic efficiency of 94%. They also proved that Mo active sites were responsible for the conversion of nitrate to nitrite, while Fe active sites further catalyzed nitrite to ammonia, with the synergistic effects improving electrochemical nitrate reduction performance.

Furthermore, various non-noble metal single atom-based catalysts have been prepared for efficient nitrate reduction, as detailed in Table 1. Most of the prepared non-noble metal single

atoms demonstrated outstanding $NH_3$ production yield and Faraday efficiency, suggesting that non-noble metal single atoms are promising candidates for electrochemical ammonia synthesis and sustainable hydrogen storage.

### 5.5 Functional catalyst design and *in situ* techniques

The stability of SACs plays a crucial role, which depends not only on the inherent tendency of isolated atoms to migrate and aggregate, but also on the strength of their interaction with the support. As an example, Xu *et al.*[100] observed that the abundant defects in Fe–N/PC (Fe SACs coordinated with nitrogen and phosphorus on a hollow carbon polyhedron) provided anchoring sites for stable loading of Fe SACs, resulting in excellent catalyst stability, as evidenced by recycling experiments showing that the $NH_3$ yield rate and Faraday efficiencies fluctuated slightly in each cycle but essentially remained stable. In addition, heteroatom doping can alter the electronic structure of the support and further enhance the interactions with SACs. For instance, Li *et al.*[140] reported that an S, N-codoped carbon basal plane could modify the coordination environment between Fe SACs and supports, create numerous defects, optimize the electronic structure of the metal atom center, and enhance the interactions between Fe SACs and the S,N-codoped carbon basal plane. These effects are crucial for improving the electrochemical nitrate reduction performance and enhancing the stability of SACs in the Fe SACs/S,N-codoped carbon basal plane system. Therefore, defect engineering and heteroatom doping of the support represent key strategies for improving the long-term durability of SACs in electrochemical nitrate reduction processes.

Furthermore, the coordination environment, supporting effects, atomic distribution, and reaction conditions also affect the electrochemical nitrate reduction performance. Based on the above discussion, the design principles of functional SACs are summarized. The selection of central metal atoms is crucial since it is closely linked to the electronic structure and catalytic performance. In addition, the conventional type of coordinating atom ($M–N_4$) of SACs can be changed by introducing heteroatoms to break the symmetric coordination structure, and thereby the electronic structure of the central site is optimized through the construction of an asymmetric active center, resulting in the improvement of the catalytic performance.[141] The support of SACs must satisfy several key requirements, including strong interactions between the metal atom and the support, precise control of the loading amount of SACs to prevent migration and aggregation, and enhancing the utilization efficiency of metal atoms during catalytic reactions.[142] In addition, the HER can be suppressed through the enhancement of the adsorption and activation efficiency of nitrate, which can be further regulated through the modulation of the electronic structure and active sites of SACs. However, it's worth noting that the reaction characteristics of different metal atoms described above are not universally applicable, as there may be differences between different systems. Electrochemical nitrate reduction by SACs involves the interplay of various factors such as the properties of SACs (*e.g.*, the type of metal atom, the

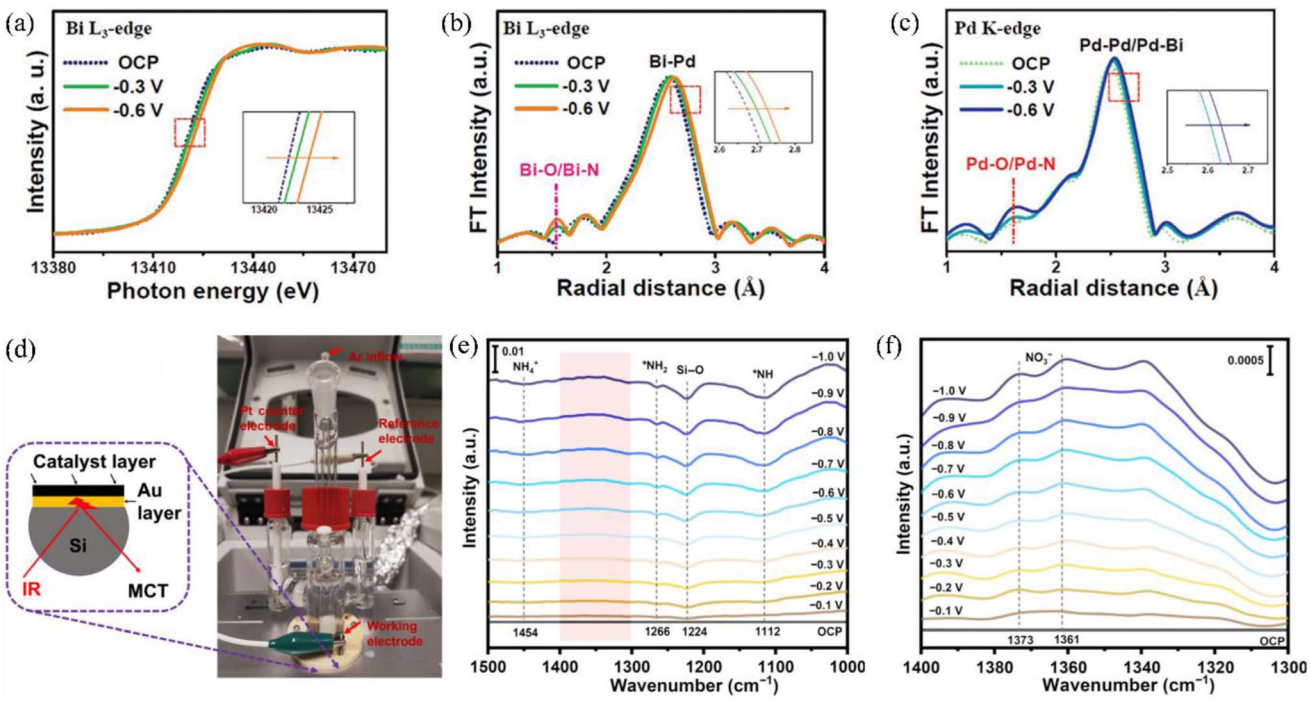


Fig. 11 (a) *Operando* Bi $L_3$-edge XANES, (b) EXAFS spectra of $Bi_1Pd$ in $NO_3^-$-containing electrolyte from open circuit potential (OCP) to −0.6 V, and (c) *operando* Pd K-edge EXAFS spectra of $Bi_1Pd$ from OCP to −0.6 V, reproduced with permission.[133] Copyright 2023, Wiley-VCH. (d) Schematic illustration of an attenuated total reflection (ATR) cell, and (e and f) *in-situ* ATR-SEIRAS of Fe SAC/NC, reproduced with permission.[135] Copyright 2024, Tsinghua University Press.

loading amount, the coordination environment, and atomic distribution), the support materials, and reaction conditions (*e.g.*, electrolyte, potential, and nitrate concentration).

As discussed in the characterization section, *in situ* techniques play a key role in the comprehensive investigation of the involved mechanisms. Therefore, this section provides a detailed discussion of the application of *operando* XAS and *in situ* FTIR during electrochemical nitrate reduction by non-noble metal single atoms. As illustrated in Fig. 11a–c, Chen *et al.*[133] performed *operando* XAS for the investigation of electronic structures and valence states of Bi SAC alloyed Pd metallenes ($Bi_1Pd$). As shown in Fig. 11a, the adsorption edge of Bi $L_3$-edge spectra shifted to a higher energy position with more negative potential, resulting in the increase of the Bi valence state, which may be attributed to electron transfer from Bi to $NO_3^-$ and related intermediates. As shown in Fig. 11b, the new Bi–O/Bi–N peak at 1.52 Å at a more negative potential was correlated with the interaction between Bi and $NO_3^-$/intermediates. The elongated Bi–Pd bond also confirmed the distortion of the Bi–Pd bond configuration, suggesting the favorable adsorption of $NO_3^-$/intermediates. Similarly, the increased intensity of the Pd–O/Pd–N bond and elongated Pd–Pd/Pd–Bi bond was also observed in Fig. 11c. These *operando* XAS results confirmed that both Bi and Pd sites are active for the electrochemical nitrate reduction process. In another study, Cheng *et al.*[135] investigated the intermediates formed using an Fe SACs/nitrogen-carbon nanonetwork (Fe SAC/NC) through *in-situ* ATR-surface-enhanced infrared absorption spectroscopy (ATR-SEIRAS) (Fig. 11d–f). As shown in Fig. 11e, three peaks at 1266 $cm^{-1}$, 1112 $cm^{-1}$, and 1454 $cm^{-1}$ were ascribed to the intermediates of $*NH_2$, *NH, and $NH_4^+$, respectively. Two upward absorption bands emerge at 1373 $cm^{-1}$ and 1361 $cm^{-1}$, related to the N–O symmetric and asymmetric stretching vibrations of $NO_3^-$, respectively (Fig. 11f). These results suggest the continuous conversion of $NO_3^-$ and generation of intermediates during the electrochemical nitrate reduction process. In conclusion, more research should focus on *in situ* techniques to investigate the underlying mechanisms during electrochemical nitrate reduction.

# 6 Conclusions and perspectives

Electrochemical nitrate reduction to ammonia has emerged as a promising strategy to simultaneously achieve nitrate-containing wastewater treatment and production of high value products. To this end, single-atom catalysts (SACs) play important roles for electrocatalysis due to their superior atom-utilization efficiency and ultrahigh catalytic performance. The present review focuses on non-noble metal SACs for electrochemical nitrate reduction to ammonia. Different synthesis methods (*e.g.*, wet chemical methods, atomic layer deposition, electrodeposition, pyrolysis, and ball-milling) for non-noble metal single-atom catalysts are comprehensively summarized. Subsequently, advanced characterization techniques including STEM, XAS, and XPS are discussed to identify the structures and properties of non-noble metal SACs. Then the performance (*e.g.*, $NH_3$ yield and faradaic efficiency) and mechanisms of electrochemical nitrate reduction by various non-noble metal SACs (*e.g.*, Fe SACs, Cu SACs, and Ni SACs) are examined. Finally, the existing challenges and future perspectives of electrochemical nitrate reduction by non-noble metal single-atom catalysts are presented as follows.

(1) Although different methods for synthesizing non-noble metal SACs have been developed, most involve complicated processes and/or require high energy consumption, making it challenging to prepare non-noble metal SACs efficiently on a large scale. In addition, the stability of non-noble metal SACs needs to be further improved since they are easily inactivated by migration and aggregation. The properties of supports, including type, surface functional group, surface charge, and specific surface area, can also significantly affect the performance of non-noble metal SACs. To complicate this, the structures and coordination environments of non-noble metal SACs can only be characterized using specialized techniques (Section 4). In summary, while non-noble metal SACs as emerging and promising catalysts present excellent catalytic performance, key issues persist to hamper their widespread implementation, such as complex synthesis, low metal loading, low stability, and low reproducibility. More research focusing on these aspects is needed.

(2) The conversion of $NO_3^-{}_{(ads)}$ to $NO_2^-{}_{(ads)}$ is widely regarded as the rate-limiting step during the electrochemical nitrate reduction process, and the binding states of intermediates can significantly affect the final products and catalytic performance. In this regard, the strong adsorption of nitrate by non-noble metal SACs is predominant due to its role in initializing the $NO_3^-{}_{(ads)}$ to $NO_2^-{}_{(ads)}$ reaction. In addition, the stabilization of intermediates (*e.g.*, $NO_2^-$) by non-noble metal SACs also plays a key role in the improvement of $NH_3$ production efficiency and selectivity, which is mainly due to the release of intermediates into electrolytes further restricting the generation and selection for $NH_3$. The strong adsorption of nitrate and intermediates by non-noble metal SACs can be achieved through functional modification, such as constructing more active sites through defect engineering or heteroatom doping, and the regulation of coordination environments and electronic structures of non-noble metal SACs.

(3) During electrochemical nitrate reduction, various operation parameters, including type, temperature and pH of electrolyte, loading amount of catalysts, applied potential, and concentration of nitrate, play predominant roles in efficient nitrate conversion. At present, most of the research focuses on the improvement of $NH_3$ yield, faradaic efficiency, and selectivity through the optimization of various operation parameters. However, the optimized conditions can also significantly affect some other properties of catalysts. For instance, reaction temperature and solution pH can affect the stability and lifetime of the catalysts. Also, the loading of catalysts and nitrate concentration are also closely tied to ecological and environmental effects. In addition, long reaction time and high applied potential can also lead to higher overall costs. Therefore, electrochemical nitrate reduction performance of non-noble metal SACs should be comprehensively evaluated from all

 

pertinent angles (*e.g.*, $NH_3$ yield, faradaic efficiency, selectivity, ecological and environmental effects, and overall costs).

(4) The mechanisms underlying electrochemical nitrate reduction by non-noble metal SACs remain incompletely understood. DFT calculations could simulate electrochemical nitrate reduction through calculating the free energy of reaction steps and adsorption energy of intermediates. However, electrochemical nitrate reduction involves multiple intermediates (*e.g.*, $N_2$, NO, and $H_2$), and slight adjustments of operating conditions can significantly change the performance, making it challenging for DFT to accurately predict electrochemical nitrate reduction by non-noble metal SACs. To address this, advanced *in situ* characterization techniques can be applied to identify changes in the electrodes, generation of products, and reaction pathways in real time, which can provide valuable insights into the involved mechanisms. However, *in situ* characterization techniques for electrochemical nitrate reduction by non-noble metal SACs are still in the infant stage, and more research should be devoted to such techniques. The combination of DFT calculations and *in situ* characterization techniques is crucial to fully understand the underlying mechanisms.

(5) At present, most of the research focuses on artificial wastewater, while practical nitrate-containing wastewater typically contains various ions and organic pollutants. Hence, additional side reactions may inhibit nitrate conversion efficiency. For instance, organic pollutants in wastewater can be oxidized or reduced and can compete for the active sites of electrodes and free electrons, compromising nitrate reduction efficiency. The presence of ions and organic pollutants can also affect the conductivity of solutions, and high applied potential is required in cases of high resistance. In addition, the detection and identification of final products are challenging due to the complex compositions of real nitrate-containing wastewater. Investigations using real wastewater would make the results more useful for eventual deployment.

(6) Currently, electrochemical nitrate reduction by non-noble metal SACs is mostly carried out at the lab-scale using synthesized nitrate-containing wastewater. Translating such results to real-world industrial scales poses a major challenge. In general, H-type cells with ion-exchange membranes are widely used for this reaction, but scaling up would involve extremely high costs and operational difficulties in the refreshing of electrolyte, collection of products, and modification flexibility. Although single cells may solve the above issues, they are not suitable for product collection and precise analysis. In this regard, flow cells are promising due to suitability for scale-up and continuous operation and high reaction rate and $NH_3$ yield. Therefore, in view of large-scale implementation, it is necessary to explore and develop novel reactors tailored for electrochemical nitrate reduction, maximize $NH_3$ yield and faradaic efficiency, and reduce the overall costs and environmental impact.

## Author contributions

Yongtao Xue: conceptualization, investigation, methodology, validation, formal analysis, data curation, writing – original draft, writing – review & editing. Xiufang He: investigation, data curation, formal analysis, writing – original draft. Jia Wei Chew: validation, writing – review & editing, funding acquisition, project administration, supervision, resources.

## Conflicts of interest

There are no conflicts to declare.

## Data availability

No primary research results and no new data were generated as part of this review.

## Acknowledgements

Y. Xue and J. W. Chew are grateful for funding from the Swedish Research Council (VR; 2025-07412) and Chalmers Gender Initiative for Excellence (Genie). X. He wishes to acknowledge funding from the Italian Ministry of Environment and Energy Sustainability (MASE, F57G25000180006).

## References

1 B. Yang, W. Ding, H. Zhang and S. Zhang, *Energy Environ. Sci.*, 2021, **14**, 672–687.
2 Y. Xiong, Y. Wang, J. Zhou, F. Liu, F. Hao and Z. Fan, *Adv. Mater.*, 2024, **36**, 2304021.
3 R. Nittoor-Veedu, X. Ju and M. Pumera, *Adv. Energy Mater.*, 2025, **15**, 2402205.
4 T. Wu, W. Fan, Y. Zhang and F. Zhang, *Mater. Today Phys.*, 2021, **16**, 100310.
5 S. M. Ghoreishian, K. Shariati, Y. S. Huh and J. Lauterbach, *Chem. Eng. J.*, 2023, **467**, 143533.
6 Y. Qin, J. Gao and B. Huang, *J. Am. Chem. Soc.*, 2025, **147**, 29673–29678.
7 A. P. Hamsa, M. Arulprakasam and S. M. Unni, *Chem. Commun.*, 2023, **59**, 10689–10710.
8 L. Wang, M. Xia, H. Wang, K. Huang, C. Qian, C. T. Maravelias and G. A. Ozin, *Joule*, 2018, **2**, 1055–1074.
9 I. M. ul Hasan, N. Xu, Y. Liu, M. Z. Nawaz, H. Feng and J. Qiao, *Electrochem. Energy Rev.*, 2024, **7**, 36.
10 H. Huang, K. Peramaiah and K.-W. Huang, *Energy Environ. Sci.*, 2024, **17**, 2682–2685.
11 K. Zhang, P. Sun, Y. Huang, M. Tang, X. Zou, Z. Pan, X. Huo, J. Wu, C. Lin, Z. Sun, Y. Wan, X. Zhang and L. An, *Adv. Funct. Mater.*, 2024, **34**, 2405179.
12 Y. Hua, N. Song, Z. Wu, Y. Lan, H. Luo, Q. Song and J. Yang, *Adv. Funct. Mater.*, 2024, **34**, 2314461.
13 M. Zhang, Z. Zhang, S. Zhang, Z. Zhuang, K. Song, K. Paramaiah, M. Yi, H. Huang and D. Wang, *ACS Catal.*, 2024, **14**, 10437–10446.
14 Y. Xiong, Y. Wang, C. C. Tsang, J. Zhou, F. Hao, F. Liu, J. Wang, S. Xi, J. Zhao and Z. Fan, *Environ. Sci. Technol.*, 2024, **58**, 10863–10873.
15 C. Feng, H. Wu, J. Shao, Q. Huo, A. Hassan, H. Yang, Q. Hu and C. He, *Adv. Energy Mater.*, 2025, **15**, 2403354.

16 Y. Shi, L. Chen, L. Xiong, X. Wang, Y. Yu and M. Yang, *Chem. Eng. J.*, 2025, **507**, 160393.
17 J. Song, S. Qian, W. Yang, J. Mu, J. Li, Y. Liu, F. Sun, S. Yu, F. Xu, X. Song, D. Deng, Y. Wang, L. Yan and Y. Ding, *Adv. Funct. Mater.*, 2024, **34**, 2409089.
18 T. S. Bui, Z. Ma, W. Zhong, G. Alfaza, P. V Kumar, S. Zhou, Y. Yang, Y. Li, R. Daiyan, E. Lovell, L. Dai and R. Amal, *Appl. Catal. B Environ. Energy*, 2026, **382**, 125954.
19 Y. Wang, J. Li, X. Xing, Y. Lv, W. Xiong, R. Lyu and H. Li, *ACS Sustain. Chem. Eng.*, 2025, **13**, 6875–6899.
20 Y. Xue and J. W. Chew, *J. Mater. Chem. A Mater.*, 2025, **13**, 11989–12008.
21 G. Wang, Z. Chen, J. Xie, L. Ding, J. Zhu, W. Wei, Y.-M. Yan, D. Chu and B.-J. Ni, *Coord. Chem. Rev.*, 2025, **539**, 216751.
22 S. Eon Jun, S. Choi, J. Kim, K. C. Kwon, S. H. Park and H. W. Jang, *Chin. J. Catal.*, 2023, **50**, 195–214.
23 W. Song, L. Yue, X. Fan, Y. Luo, B. Ying, S. Sun, D. Zheng, Q. Liu, M. S. Hamdy and X. Sun, *Inorg. Chem. Front.*, 2023, **10**, 3489–3514.
24 X. Lu, H. Song, J. Cai and S. Lu, *Electrochem. commun.*, 2021, **129**, 107094.
25 Y. Feng, J.-T. Ren, M.-L. Sun and Z.-Y. Yuan, *Chem. Sci.*, 2025, **16**, 1528–1559.
26 D. Liu, L. Qiao, S. Peng, H. Bai, C. Liu, W. F. Ip, K. H. Lo, H. Liu, K. W. Ng, S. Wang, X. Yang and H. Pan, *Adv. Funct. Mater.*, 2023, **33**, 2303480.
27 T. Ren, Y. Sheng, M. Wang, K. Ren, L. Wang and Y. Xu, *Chin. J. Struct. Chem.*, 2022, **41**, 2212089–2212106.
28 Y. Li, C. J. Miller, L. Wu and T. D. Waite, *Environ. Sci. Technol.*, 2022, **56**, 5820–5829.
29 X. Zou, J. Xie, C. Wang, G. Jiang, K. Tang and C. Chen, *Chin. Chem. Lett.*, 2023, **34**, 107908.
30 A. MariaJoseph, S. Nangan, D. Verma, L. Gnanasekaran, S. Rajendran, T. Natesan, P. Pattananuwat and M. Okhawilai, *Fuel*, 2024, **367**, 131408.
31 V. T. Chebrolu, D. Jang, G. M. Rani, C. Lim, K. Yong and W. B. Kim, *Carbon Energy*, 2023, **5**, e361.
32 T. Takashima, T. Mochida and H. Irie, *Sustain. Energy Fuels*, 2023, **7**, 2740–2748.
33 B. Jiang, Y. Pan, Y. Tan, A. Li, C. Shuang and F. Liu, *J. Ind. Eng. Chem.*, 2024, **136**, 359–367.
34 S. Li, D. Han, G. Jiang, Z. Han, H. Lu, J. Gao, X. Wang, Y. Wang, C. Geng, Z. Weng and Q.-H. Yang, *ACS Appl. Energy Mater.*, 2023, **6**, 5067–5073.
35 R. Boppella, M. Ahmadi, B. M. Arndt, D. R. Lustig and M. Nazemi, *ACS Catal.*, 2024, **14**, 18223–18236.
36 F.-Y. Chen, A. Elgazzar, S. Pecaut, C. Qiu, Y. Feng, S. Ashokkumar, Z. Yu, C. Sellers, S. Hao, P. Zhu and H. Wang, *Nat. Catal.*, 2024, **7**, 1032–1043.
37 Y. Li, Y. Zhou, C. Shang, M. Yousaf, Z. Guo and S. Guo, *Acc. Mater. Res.*, 2022, **3**, 1160–1172.
38 Q.-N. Zhan, T.-Y. Shuai, H.-M. Xu, C.-J. Huang, Z.-J. Zhang and G.-R. Li, *Chin. J. Catal.*, 2023, **47**, 32–66.
39 Y. Sun, X. Liu, M. Zhu, Z. Zhang, Z. Chen, S. Wang, Z. Ji, H. Yang and X. Wang, *DeCarbon*, 2023, **2**, 100018.
40 D. Wang, Z. Yuan, X. Wu, W. Xiong, J. Ding, Z. Zhang and W. Huang, *ACS Catal.*, 2023, **13**, 7132–7138.
41 L. Zeng, J.-W. Chen, L. Zhong, W. Zhen, Y. Y. Tay, S. Li, Y.-G. Wang, L. Huang and C. Xue, *Appl. Catal. B Environ. Energy*, 2022, **307**, 121154.
42 F. Zhang, Y. Zhu, Q. Lin, L. Zhang, X. Zhang and H. Wang, *Energy Environ. Sci.*, 2021, **14**, 2954–3009.
43 J. Fonseca and J. Lu, *ACS Catal.*, 2021, **11**, 7018–7059.
44 X. Wang, B. Jin, Y. Jin, T. Wu, L. Ma and X. Liang, *ACS Appl. Nano Mater.*, 2020, **3**, 2867–2874.
45 P. E. Imoisili, J. Ren and T.-C. Jen, *Electrochem. commun.*, 2022, **135**, 107215.
46 C. Wang, Y. Kong, M. Soldemo, Z. Wu, H. Tissot, B. Karagoz, K. Marks, J. H. Stenlid, A. Shavorskiy, E. Kokkonen, S. Kaya, D. J. Stacchiola and J. Weissenrieder, *Chem. Mater.*, 2022, **34**, 2313–2320.
47 L. Zhang, R. Si, H. Liu, N. Chen, Q. Wang, K. Adair, Z. Wang, J. Chen, Z. Song, J. Li, M. N. Banis, R. Li, T.-K. Sham, M. Gu, L.-M. Liu, G. A. Botton and X. Sun, *Nat. Commun.*, 2019, **10**, 4936.
48 Q. Yang, Y. Jiang, H. Zhuo, E. M. Mitchell and Q. Yu, *Nano Energy*, 2023, **111**, 108404.
49 M. S. Iqbal, Z.-B. Yao, Y.-K. Ruan, R. Iftikhar, L.-D. Hao, A. W. Robertson, S. M. Imran and Z.-Y. Sun, *Rare Metals*, 2023, **42**, 1075–1097.
50 Z. Shixuan, L. Donghao, J. Jiwei, F. Li and T. Hua, *Electrochim. Acta*, 2023, **437**, 141543.
51 Q. Zhao, Y. Wang, M. Li, S. Zhu, T. Li, J. Yang, T. Lin, E. P. Delmo, Y. Wang, J. Jang, M. Gu and M. Shao, *SmartMat*, 2022, **3**, 183–193.
52 J. Xu, R. Li, C.-Q. Xu, R. Zeng, Z. Jiang, B. Mei, J. Li, D. Meng and J. Chen, *Appl. Catal. B*, 2021, **289**, 120028.
53 X. Gao, Q. Dai, X. Lu and S. Kawi, *Int. J. Hydrogen Energy*, 2023, **48**, 17106–17136.
54 M. Li, J. Yu, Q. Liu, J. Liu, R. Chen, J. Zhu, R. Li and J. Wang, *ACS Sustain. Chem. Eng.*, 2022, **10**, 13505–13513.
55 Y. Guo, S. Yao, Y. Xue, X. Hu, H. Cui and Z. Zhou, *Appl. Catal. B*, 2022, **304**, 120997.
56 C. Zhu, Y. Nie, F. Cun, Y. Wang, Z. Tian and F. Liu, *Appl. Catal. B*, 2022, **319**, 121900.
57 J. W. Lim, D. H. Choo, J. H. Cho, J. Kim, W. S. Cho, O. F. Ngome Okello, K. Kim, S. Lee, J. Son, S.-Y. Choi, J. K. Kim, H. W. Jang, S. Y. Kim and J.-L. Lee, *J. Mater. Chem. A Mater.*, 2024, **12**, 11090–11100.
58 H. Zhang, G. Guo, Z. Wang, X. He and H. Ji, *Ind. Eng. Chem. Res.*, 2024, **63**, 19530–19536.
59 H. Xu, L. Zhang, H. Wang, S. Zhang, W. Li, X. Wang, S. Song, D. Wang and Z. Shi, *Chem. Res. Chin. Univ.*, 2023, **39**, 948–953.
60 R. Tang, H. Wang, X. Dong, S. Zhang, L. Zhang and F. Dong, *J. Colloid Interface Sci.*, 2023, **630**, 290–300.
61 T. Liu, F. Sun, M. Huang and L. Guan, *Mater. Adv.*, 2022, **3**, 1565–1573.
62 X. Mao, Z. Deng, Y. Liu, H. Xie, Q. He, Y. Zhang, Z. Huang, H. Hu and T. Gan, *Appl. Surf. Sci.*, 2022, **597**, 153625.
63 F. Li, G.-F. Han, W. Che, J.-M. Seo, W. Zou, H. Liu, I. Ahmad, Z. Fu, Y. Lu and J.-B. Baek, *Nano Energy*, 2023, **114**, 108647.

 

64 X. Zhang, Y. Zhong, H. Chen, Y. Cheng, Q. Sun, H. Zhang, Q. He, Y. Zhang, G. Guo, X. He and H. Ji, *Chem. Res. Chin. Univ.*, 2022, **38**, 1258–1262.
65 J. Xi, H. S. Jung, Y. Xu, F. Xiao, J. W. Bae and S. Wang, *Adv. Funct. Mater.*, 2021, **31**, 2008318.
66 H. Zhang, Y. Dong, S. Zhao, G. Wang, P. Jiang, J. Zhong and Y. Zhu, *Appl. Catal. B*, 2020, **261**, 118233.
67 X. Zhao, X. Zheng, Q. Lu, Y. Li, F. Xiao, B. Tang, S. Wang, D. Y. W. Yu and A. L. Rogach, *EcoMat*, 2023, **5**, e12293.
68 M. Wen, N. Sun, L. Jiao, S.-Q. Zang and H.-L. Jiang, *Angew. Chem., Int. Ed.*, 2024, **63**, e202318338.
69 B. Wang, J. Tang, X. Zhang, M. Hong, H. Yang, X. Guo, S. Xue, C. Du, Z. Liu and J. Chen, *Chem. Eng. J.*, 2022, **437**, 135295.
70 Y. Chen, J. Li, N. Wang, Y. Zhou, J. Zheng and W. Chu, *Chem. Eng. J.*, 2022, **448**, 137611.
71 P. Rao, D. Wu, J. Luo, J. Li, P. Deng, Y. Shen and X. Tian, *Cell Rep. Phys. Sci.*, 2022, **3**(5), 100880.
72 C. Jia, S. Li, Y. Zhao, R. K. Hocking, W. Ren, X. Chen, Z. Su, W. Yang, Y. Wang, S. Zheng, F. Pan and C. Zhao, *Adv. Funct. Mater.*, 2021, **31**, 2107072.
73 R. Chen, S. Chen, L. Wang and D. Wang, *Adv. Mater.*, 2024, **36**, 2304713.
74 X. Jiang, L. Tang, L. Dong, X. Sheng, W. Zhang, Z. Liu, J. Shen, H. Jiang and C. Li, *Angew. Chem., Int. Ed.*, 2023, **62**, e202307848.
75 S. Ma, W. Han, W. Han, F. Dong and Z. Tang, *J. Mater. Chem. A Mater.*, 2023, **11**, 3315–3363.
76 X. Bai and J. Guan, *Small Struct.*, 2023, **4**, 2200354.
77 X. Wang, Y. Zhang, J. Wu, Z. Zhang, Q. Liao, Z. Kang and Y. Zhang, *Chem. Rev.*, 2022, **122**, 1273–1348.
78 B. Guo, Z. Wang, L. Zheng, G. Mo, H. Zhou and D. Luo, *Carbon Energy*, 2024, **6**, e554.
79 C. Guo, Y. Cao, Y. Gao, C. Zhi, Y.-X. Wang, Y. Luo, X.-J. Yang and X. Luo, *Adv. Funct. Mater.*, 2024, **34**, 2314189.
80 A. M. Agour, E. Elkersh, G. E. Khedr, H. G. El-Aqapa and N. K. Allam, *ACS Appl. Nano Mater.*, 2023, **6**, 15980–15989.
81 Z. Lang, X. Wang, S. Jabeen, Y. Cheng, N. Liu, Z. Liu, T. Gan, Z. Zhuang, H. Li and D. Wang, *Adv. Mater.*, 2025, **37**, 2418942.
82 D. Deng, X. Chen, L. Yu, X. Wu, Q. Liu, Y. Liu, H. Yang, H. Tian, Y. Hu and P. Du, *Sci. Adv.*, 2015, **1**, e1500462.
83 X. Zhou, R. Xia, Y. Wang, M. Xing, L. Zhang and H. Cao, *Surfaces and Interfaces*, 2025, **72**, 107119.
84 R. T. Hannagan, G. Giannakakis, R. Réocreux, J. Schumann, J. Finzel, Y. Wang, A. Michaelides, P. Deshlahra, P. Christopher, M. Flytzani-Stephanopoulos, M. Stamatakis and E. C. H. Sykes, *Science*, 2021, **372**, 1444–1447.
85 S.-M. Wu and P. Schmuki, *Adv. Mater.*, 2025, **37**, 2414889.
86 M. Agrachev, V. Giulimondi, I. Surin, S. Mitchell, G. Jeschke and J. Pérez-Ramírez, *Chem Catalysis*, DOI: 10.1016/j.checat.2024.101136.
87 G. Zichittella, Y. Polyhach, R. Tschaggelar, G. Jeschke and J. Pérez-Ramírez, *Angew. Chem., Int. Ed.*, 2021, **60**, 3596–3602.
88 Z. Li, S. Ji, C. Xu, L. Leng, H. Liu, J. H. Horton, L. Du, J. Gao, C. He, X. Qi, Q. Xu and J. Zhu, *Adv. Mater.*, 2023, **35**, 2209644.
89 Y. Li, Y. Ji, Y. Zhao, J. Chen, S. Zheng, X. Sang, B. Yang, Z. Li, L. Lei, Z. Wen, X. Feng and Y. Hou, *Adv. Mater.*, 2022, **34**, 2202240.
90 Y. Shang, X. Duan, S. Wang, Q. Yue, B. Gao and X. Xu, *Chin. Chem. Lett.*, 2022, **33**, 663–673.
91 Y. Li, H. Sun, L. Ren, K. Sun, L. Gao, X. Jin, Q. Xu, W. Liu and X. Sun, *Angew. Chem., Int. Ed.*, 2024, **63**, e202405334.
92 C. Mu, C. Lv, X. Meng, J. Sun, Z. Tong and K. Huang, *Adv. Mater. Interfaces*, 2023, **10**, 2201842.
93 C. Hu, Y. Hu, B. Zhang, H. Zhang, X. Bao, J. Zhang and P. Yuan, *Electrochem. Energy Rev.*, 2024, **7**, 19.
94 X.-M. Lin, X.-T. Yang, H.-N. Chen, Y.-L. Deng, W.-H. Chen, J.-C. Dong, Y.-M. Wei and J.-F. Li, *J. Energy Chem.*, 2023, **76**, 146–164.
95 Y. Wang, C. Wang, M. Li, Y. Yu and B. Zhang, *Chem. Soc. Rev.*, 2021, **50**, 6720–6733.
96 X. Song, L. Xu, X. Sun and B. Han, *Sci. China Chem.*, 2023, **66**, 315–323.
97 Z.-Y. Wu, M. Karamad, X. Yong, Q. Huang, D. A. Cullen, P. Zhu, C. Xia, Q. Xiao, M. Shakouri, F.-Y. Chen, J. Y. (Timothy) Kim, Y. Xia, K. Heck, Y. Hu, M. S. Wong, Q. Li, I. Gates, S. Siahrostami and H. Wang, *Nat. Commun.*, 2021, **12**, 2870.
98 P. Li, Z. Jin, Z. Fang and G. Yu, *Energy Environ. Sci.*, 2021, **14**, 3522–3531.
99 L. Liu, T. Xiao, H. Fu, Z. Chen, X. Qu and S. Zheng, *Appl. Catal. B*, 2023, **323**, 122181.
100 J. Xu, S. Zhang, H. Liu, S. Liu, Y. Yuan, Y. Meng, M. Wang, C. Shen, Q. Peng, J. Chen, X. Wang, L. Song, K. Li and W. Chen, *Angew. Chem., Int. Ed.*, 2023, **62**, e202308044.
101 W.-D. Zhang, H. Dong, L. Zhou, H. Xu, H.-R. Wang, X. Yan, Y. Jiang, J. Zhang and Z.-G. Gu, *Appl. Catal. B*, 2022, **317**, 121750.
102 W. Cao, J. Nie, Y. Cao, C. Gao, M. Wang, W. Wang, X. Lu, X. Ma and P. Zhong, *Chem. Eng. J.*, 2024, **496**, 154097.
103 Y. Ren, F. Tian, L. Jin, Y. Wang, J. Yang, S. You and Y. Liu, *Environ. Sci. Technol.*, 2023, **57**, 10458–10466.
104 E. Murphy, B. Sun, M. Rüscher, Y. Liu, W. Zang, S. Guo, Y.-H. Chen, U. Hejral, Y. Huang, A. Ly, I. V Zenyuk, X. Pan, J. Timoshenko, B. R. Cuenya, E. D. Spoerke and P. Atanassov, *Adv. Mater.*, 2024, **36**, 2401133.
105 Z. Wang, S. Liu, X. Zhao, M. Wang, L. Zhang, T. Qian, J. Xiong, C. Yang and C. Yan, *ACS Mater. Lett.*, 2023, **5**, 1018–1026.
106 H. Chen, C. Zhang, L. Sheng, M. Wang, W. Fu, S. Gao, Z. Zhang, S. Chen, R. Si, L. Wang and B. Yang, *J. Hazard. Mater.*, 2022, **434**, 128892.
107 X. Zhao, Q. Geng, F. Dong, K. Zhao, S. Chen, H. Yu and X. Quan, *Chem. Eng. J.*, 2023, **466**, 143314.
108 H. Yin, F. Dong, H. Su, Z. Zhuang, Y. Wang, D. Wang, Y. Peng and J. Li, *ACS Nano*, 2023, **17**, 25614–25624.
109 Y. Zuo, M. Sun, T. Li, L. Sun, S. Han, Y. Chai, B. Huang and X. Wang, *Adv. Mater.*, 2025, **37**, 2415632.

110 Y. Liu, J. Wei, Z. Yang, L. Zheng, J. Zhao, Z. Song, Y. Zhou, J. Cheng, J. Meng, Z. Geng and J. Zeng, *Nat. Commun.*, 2024, **15**, 3619.
111 Y. Liu, W. Qiu, P. Wang, R. Li, K. Liu, K. M. Omer, Z. Jin and P. Li, *Appl. Catal. B*, 2024, **340**, 123228.
112 X.-F. Cheng, J.-H. He, H.-Q. Ji, H.-Y. Zhang, Q. Cao, W.-J. Sun, C.-L. Yan and J.-M. Lu, *Adv. Mater.*, 2022, **34**, 2205767.
113 J. Yang, H. Qi, A. Li, X. Liu, X. Yang, S. Zhang, Q. Zhao, Q. Jiang, Y. Su, L. Zhang, J.-F. Li, Z.-Q. Tian, W. Liu, A. Wang and T. Zhang, *J. Am. Chem. Soc.*, 2022, **144**, 12062–12071.
114 Y.-T. Xu, M.-Y. Xie, H. Zhong and Y. Cao, *ACS Catal.*, 2022, **12**, 8698–8706.
115 S. Ajmal, A. Kumar, M. A. Mushtaq, M. Tabish, Y. Zhao, W. Zhang, A. S. Khan, A. Saad, G. Yasin and W. Zhao, *Small*, 2024, **20**, 2310082.
116 X. Zhao, Z. Zhu, Y. He, H. Zhang, X. Zhou, W. Hu, M. Li, S. Zhang, Y. Dong, X. Hu, A. V Kuklin, G. V Baryshnikov, H. Ågren, T. Wågberg and G. Hu, *Chem. Eng. J.*, 2022, **433**, 133190.
117 Z. Xi, J. Wang, B. Liu, X. Xu, P. Jing, R. Gao and J. Zhang, *J. Energy Chem.*, 2023, **83**, 32–42.
118 C. He, Y. Gong, S. Li, J. Wu, Z. Lu, Q. Li, L. Wang, S. Wu and J. Zhang, *Adv. Mater.*, 2024, **36**, 2311628.
119 Q. Gao, X. Han, Y. Liu and H. Zhu, *ACS Catal.*, 2024, **14**, 6045–6061.
120 J. Cai, Y. Wei, A. Cao, J. Huang, Z. Jiang, S. Lu and S.-Q. Zang, *Appl. Catal. B*, 2022, **316**, 121683.
121 S. Zhang, Y. Zha, Y. Ye, K. Li, Y. Lin, L. Zheng, G. Wang, Y. Zhang, H. Yin, T. Shi and H. Zhang, *Nanomicro Lett.*, 2023, **16**, 9.
122 J. Zhao, X. Ren, X. Liu, X. Kuang, H. Wang, C. Zhang, Q. Wei and D. Wu, *Chem. Eng. J.*, 2023, **452**, 139533.
123 L. Yang, C. Wang, Y. Li, W. Ge, L. Tang, J. Shen, Y. Zhu and C. Li, *Adv. Funct. Mater.*, 2024, **34**, 2401094.
124 N. Zhang, J. Shang, X. Deng, L. Cai, R. Long, Y. Xiong and Y. Chai, *ACS Nano*, 2022, **16**, 4795–4804.
125 W. Zhang, S. Zhan, J. Xiao, T. Petit, C. Schlesiger, M. Mellin, J. P. Hofmann, T. Heil, R. Müller, K. Leopold and M. Oschatz, *Advanced Science*, 2023, **10**, 2302623.
126 Y. Zhang, B. Johannessen, P. Zhang, J. Gong, J. Ran and S.-Z. Qiao, *Adv. Mater.*, 2023, **35**, 2306923.
127 Y. Wang, H. Yin, F. Dong, X. Zhao, Y. Qu, L. Wang, Y. Peng, D. Wang, W. Fang and J. Li, *Small*, 2023, **19**, 2207695.
128 J. Wan, H. Zhang, J. Yang, J. Zheng, Z. Han, W. Yuan, B. Lan and X. Li, *Appl. Catal. B Environ. Energy*, 2024, **347**, 123816.
129 Y. Xue, Q. Yu, Q. Ma, Y. Chen, C. Zhang, W. Teng, J. Fan and W. Zhang, *Environ. Sci. Technol.*, 2022, **56**, 14797–14807.
130 P. Li, L. Liao, Z. Fang, G. Su, Z. Jin and G. Yu, *Proc. Natl. Acad. Sci.*, 2023, **120**, e2305489120.
131 X. Zhao, X. Jia, Y. He, H. Zhang, X. Zhou, H. Zhang, S. Zhang, Y. Dong, X. Hu, A. V Kuklin, G. V Baryshnikov, H. Ågren and G. Hu, *Appl. Mater. Today*, 2021, **25**, 101206.
132 B. Zhou, L. Yu, W. Zhang, X. Liu, H. Zhang, J. Cheng, Z. Chen, H. Zhang, M. Li, Y. Shi, F. Jia, Y. Huang, L. Zhang and Z. Ai, *Angew. Chem., Int. Ed.*, 2024, **63**, e202406046.
133 K. Chen, Z. Ma, X. Li, J. Kang, D. Ma and K. Chu, *Adv. Funct. Mater.*, 2023, **33**, 2209890.
134 W. Ye, Y. Yao, X. Wei, M. Xu, S. Zhao, W. Wang, G. Jia, F. Dai, P. Gao, X. Lu, X. Li, B. Xi, N. Wang and S. Xiong, *Angew. Chem., Int. Ed.*, 2025, **64**, e202509303.
135 X. Cheng, W. Shang, Y. Li, J. Hu, J. Guo, D. Cao, N. Zhang, S. Zhang, S. Song, T. Liu, W. Liu and Y. Shi, *Nano Res.*, 2024, **17**, 6826–6832.
136 X. Lu, J. Wei, H. Lin, Y. Li and Y. Li, *ACS Appl. Nano Mater.*, 2024, **7**, 14654–14664.
137 Z. Gu, Y. Zhang, Y. Fu, D. Hu, F. Peng, Y. Tang and H. Yang, *Angew. Chem., Int. Ed.*, 2024, **63**, e202409125.
138 L. Wang, P. Guo, Y. Han, C. Han, H. Sun, R. Huang, X. Liu, M. Huang, Z. Mao, X. Yan, A. Du and X. Wang, *Chem Catal.*, 2024, **4**(4), 100936.
139 L. Xu, L. Liu, G. Chen and D. Xia, *Chin. Chem. Lett.*, 2025, 111188.
140 J. Li, M. Li, N. An, S. Zhang, Q. Song, Y. Yang and X. Liu, *Proc. Natl. Acad. Sci.*, 2021, **118**, e2105628118.
141 K. Yu, K. Zhou, S. Liang, Y. Xu, T. Luo, Y. Leng and Z. Chen, *Nano Res.*, 2026, **19**, 94908183.
142 X. Zhang, S. Li, G. Zhao, H. Zhao and M. Zhou, *Appl. Catal. B Environ. Energy*, 2025, **363**, 124783.

 